BRNO UNIVERSITY OF TECHNOLOGY

VYSOKÉ UČENÍ TECHNICKÉ V BRNĚ

FACULTY OF MECHANICAL ENGINEERING

FAKULTA STROJNÍHO INŽENÝRSTVÍ

INSTITUTE OF PHYSICAL ENGINEERING

ÚSTAV FYZIKÁLNÍHO INŽENÝRSTVÍ

INFLUENCE OF SADDLE DEFLECTION COILS INACCURACY ON IMAGE ABERRATIONS

VLIV NEPŘESNOSTI VINUTÍ SEDLOVÝCH VYCHYLOVACÍCH CÍVEK NA VADY ZOBRAZENÍ

MASTER'S THESIS

DIPLOMOVÁ PRÁCE

AUTHOR

AUTOR PRÁCE

Bc. Martin Mičulka

SUPERVISOR

VEDOUCÍ PRÁCE

Ing. Ondřej Sháněl, Ph.D.

BRNO 2021

BRNO UNIVERSITY OF TECHNOLOGY
FACULTY OF MECHANICAL ENGINEERING

Assignment Master's Thesis

Institut:	Institute of Physical Engineering
Student:	**Bc. Martin Mičulka**
Degree programm:	Physical Engineering and Nanotechnology
Branch:	no specialisation
Supervisor:	**Ing. Ondřej Sháněl, Ph.D.**
Academic year:	2021/22

As provided for by the Act No. 111/98 Coll. on higher education institutions and the BUT Study and Examination Regulations, the director of the Institute hereby assigns the following topic of Master's Thesis:

Influence of saddle deflection coils inaccuracy on image aberrations

Brief Description:

Manufacturing of deflection coils is limited in its precision by human errors or mechanical accuracy of support elements in principle. Fourier analysis of multipoles field demonstrates that misaligned saddle coils produce not only dipole deflection field but weak quadrupole field as well. Its strength depends on saddle coils excitation and an angle of their misalignment. Understanding of this dependency is crucial for definition of correction elements type and its optical strength.

Master's Thesis goals:

1. Analysis of multipole fourier components of mechanical misaligned saddle deflection unit. Derivation of quadrupole field strength based on angle of misalignment of saddle coil pair.
2. Comparison of axial multipole fields of misaligned deflector obtained with 3D FEM and with simplified 2D model.

Recommended bibliography:

REIMER, Ludwig. Scanning electron microscopy: physics of image formation and microanalysis. 2nd completely rev. and updated ed. New York: Springer, 1998. ISBN 978-3-540-63976-3.

HORÁK, Michal, Viktor BADIN a Jakub ZLÁMAL. Accurate interpolation of 3D fields in charged particle optics. Ultramicroscopy. 2018, 189, 95-101. ISSN 03043991. Dostupné z: doi:10.1016/j.ultramic.2018.03.023

Deadline for submission Master's Thesis is given by the Schedule of the Academic year 2021/22

In Brno,

L. S.

prof. RNDr. Tomáš Šikola, CSc. Director of the Institute	doc. Ing. Jaroslav Katolický, Ph.D. FME dean

Abstract
This thesis deals with computing of parasitic magnetic fields of the misaligned deflection coil due to the manufacturing imperfections. The relation between the multipole magnetic fields and the asymmetric winding distribution of an electron deflection system is discussed. Novel and fast 2D methods of calculation are introduced. The results are then compared with the 3D final elements method as well as with an experiment. Consequently, the influence of the parasitic multipole fields due to the manufacturing imperfections on astigmatism is examined.

Keywords
Deflection coil, saddle coil, manufacturing imperfections, parasitic aberrations, magnetic dipole field.

Abstrakt
Tato práce se zabývá výpočtem parazitických magnetických polí neseřízené deflekční cívky z důvodu výrobních nepřesností. Vztah mezi multipólovými magnetickými poli a asymetrickým rozložením vynutím elektronové vychylovací cívky je rozebrán. Nové a rychlé 2D metody výpočtu jsou představeny. Výsledky jsou poté porovnány s 3D metodou konečných prvků a s experimentem. Vliv multipólových parazitických polí způsobených nepřesností výroby na astigmatismus je tak v důsledku prošetřen.

Klíčová slova
Deflekční cívka, sedlová cívka, výrobní nepřesnosti, parazitická aberace, magnetické dipólové pole.

MIČULKA, M. *Influence of saddle deflection coils inaccuracy on image aberrations.* Brno: Brno University of Technology, Faculty of Mechanical Engineering, 2022. 49 p. Supervisor Ing. Ondřej Sháněl, Ph.D.

Prohlašuji, že jsem diplomovou práci s názvem "*Vliv nepřesnosti vinutí sedlových vychylovacích cívek na vady zobrazení*" vypracoval samostatně pod vedením Ing. Ondřeje Sháněla, Ph.D. a že veškerou použitou literaturu a ostatní informační zdroje uvádím v seznamu literatury.

V Brně dne 19. 5. 2022

Bc. Martin Mičulka

Acknowledgments

I want to express my sincerest thanks to my family for supporting me during my studies.

I would like to thank Ing. Ondřej Sháněl, Ph.D., for letting me study this exciting problem and for always motivating me to continue.

I would like to thank Ing. Jakub Zlámal, Ph.D., for supervising me. My thesis would be impossible to complete without his previous excellent work and help.

I would like to thank Ing. František Zelenka for providing outstanding micro-CT scans to support my work.

I would like to thank Dr. Peter Tiemeijer for sharing his theory of aberrations.

Bc. Martin Mičulka

Contents

1. Introduction

The deflection coils are types of magnetic coils used inside electron microscopes. They enable us to manipulate the trajectory of the electron beam, and they are indispensable for scanning with the electron beam over the sample or optimizing the beam position on the sample concerning the optical aberrations. Another critical use of deflection coils is an accurate adjustment of concentricity of electron-optical elements in the electron microscope. During the production process, manufacturers face the challenging procedure of accurately adjusting the mechanical parts on the optical axis in the electron microscope. Moreover, it is impossible to reach the required production precision for the concentricity of optical elements, and therefore, a solution in the form of a deflection element is required. The most crucial goal of the design process is to find an optical system with the required aberration coefficients. Deflection coils are designed in many forms, such as toroidal, Helmholtz or saddle coils. However, only saddle coils are widely used by manufacturers due to their smallest optical aberrations from all coils mentioned above. Saddle coils are convenient for generating a uniform magnetic field perpendicular to the cylinder axis.

The accuracy in the manufacturing process is always limited. Therefore, by studying the magnetic field produced by an asymmetric saddle coil with the dependency on the manufacturing precision, we could set out the conditions for a more cost-effective manufacturing process of the saddle coils for the electron beam deflection in electron microscopes. Furthermore, as a result, it would allow us to obtain a higher resolution of transmission electron microscopes for lower production costs.

Chapter 2 deals with the following areas. Brief history and the key milestones of electron microscopy are discussed. Reduced axial magnetic potentials characterize parasitic or multipole magnetic fields. Therefore, the radial expansion of the magnetic field is mentioned. Consequently, the quality of the optical system can be judged by the use of the trajectory equation. A general overview is given of the design of the transmission electron microscope and its main parts to provide a holistic perspective and set this thesis in the broader context of current challenges of design and manufacturing philosophy. Focus is given to the most widespread deflection systems and the corrector systems in the form of stigmators.

Chapter 3 introduces the reader to the calculation methods of the parasitic multipoles of the misaligned deflection coil. The infinite dipole method is brought up. However, it is only an approximation according to the top-hat model. Therefore, new and more precise methods are introduced. They are called the normalized Fourier series coefficients and the corrected multipole methods. They reduce the problem of parasitic multipoles fields of the misaligned deflection coil to the sets of perfect multipoles. Therefore, the misaligned deflection coil problem is mapped on the group of previously solved problems. Moreover, they are easy to implement in the Electron Optical Design software. 3D final elements method was chosen to validate the new approaches.

Chapter 4 is dedicated to evaluating the results of simulation methods qualitatively. Multipole fields of the misaligned saddle coil are calculated for increasing the misalignment angle by each method.

Chapter 5 brings the new simulation methods to the test in the experiment. Micro-CT is then carried out to precisely measure the misalignment of the saddle deflection coils used in the experiment. Thus, novel calculation methods are experimentally tested.

2. Theoretical part

2.1. History

The early history of electron microscopy dates back to the early 20th century. First, essential steps were laid down by a German physicist and a pioneer of electron optics, prof. Hans Busch. He suggested in 1926 that a magnetic field in the short coil could be used to focus the electron beam to a point similarly as glass lenses focus light [1].

This discovery that electrons could be used instead of photons greatly inspired a physicist Ernst Ruska when he first read about it in the academic journal *Archiv für Elektrotechnik* [2]. However, it was no straightforward task from the idea to the first electron microscope. Ruska and together with an electrical engineer Max Knoll, demonstrated the first proof of concept that the magnetic coil can work as the electron lens in 1931 [3]. Two short magnetic lenses were put together with a modest magnification of 14.4. Today this apparatus is considered the first electron microscope. At first, Ruska, and Knoll hoped that the electron microscope resolution would not be limited in the same way as it is the case of the optical microscope, which is limited by the Abbe diffraction limit and by the wavelength of light. When Ruska first found out about the controversial and not entirely accepted theory of the French physicist de Broglie that all matter, and therefore electrons, exhibits wave-like behavior, he was deeply disappointed that the electron microscope resolution is limited by the wavelength again as well. The only encouragement for Ruska was that he calculated with the help of de Broglie's theory that the maximum resolution for electron microscopy is to be about five orders of magnitude higher than of the optical microscope. So there was no reason to abandon the pursuit of electron microscopy. At that time, not many experts took Ruska's and Knoll's approach seriously, and still, many problems had to be overcome, but the time showed they were right [3].

A slight concern gave a German physicist Otto Scherzer in 1936 when he proved there is a fundamental limit to the resolution because all rotationally symmetric fields of the electron lenses have an unavoidable and always positive spherical and chromatic aberration. So, these aberrations can not be compensated by combing multiple rotationally symmetric lenses. This statement is nowadays called Scherzer's theorem. Nevertheless, Scherzer pursued the development of corrective elements for spherical and chromatic aberrations in the form of multipoles or by time-varying electromagnetic fields [4].

Vladimir K. Zworykin developed the first scanning electron microscope in the modern sense in 1942. He was the first who realized that secondary electrons could provide topographical contrast, and he managed to enhance the signal by biasing the electron collector positively relative to the specimen. He was able to reach a decent resolution of 50 nm, but it was considered low in comparison with the transmission electron microscopy [5].

Albert Crewe invented the first field emission electron source in 1968 [6]. It was an essential milestone for higher resolution because of its higher brightness and lower energy dispersion. Furthermore, with his unremitting effort, he patented and tried to unsuccessfully develop the first hexapole corrector of spherical aberration in electron optics in 1980 [7].

Max Haider and Harald Rose started the development of spherical aberration corrector in Germany in 1992. Later, Max Haider cofounded CEOS company in 1996 [8].

Finally, Ernst Ruska was awarded the Nobel Prize in Physics in 1986 "for his fundamental work in electron optics and the design of the first electron microscope." The other part of the prize was awarded to Gerd Binnig and Heinrich Rohrer for their development of another revolutionary instrument called a scanning tunneling microscope [9].

2.2. Trajectory equation

Newton's second law of motion describes a motion of an object with a mass m [10]. Net force $\vec{F}$ acting on the object produces an acceleration $\vec{a}$

$$\vec{F} = m\vec{a} = \frac{d(m\vec{v})}{dt}, \tag{2.1}$$

where $\vec{v}$ is velocity of the object and t is time. Electron in the electric $\vec{E}$ or magnetic $\vec{B}$ field is influenced by the Lorentz force [11] p. 204

$$\vec{F}_{\text{Lor}} = -e(\vec{E} + \vec{v} \times \vec{B}), \tag{2.2}$$

where e is the elementary charge. Then, equation of motion with the relativistic correction is

$$\frac{\mathrm{d}}{\mathrm{d}t}(\gamma m_0 \vec{v}) = -e(\vec{E} + \vec{v} \times \vec{B}), \tag{2.3}$$

where m_0 the rest mass and γ is the Lorentz factor [11] p. 486

$$\gamma = \frac{1}{\sqrt{1 - \frac{v^2}{c^2}}}, \tag{2.4}$$

where c is the speed of light in a vacuum. It is necessary to use the realistic correction for Newton's second law of motion because even the standard energies of 60-300 keV of TEM change the characteristics of the electron substantially compared to the classical approximation. These changes are summarized in the table 2.1.

Table 2.1: The relativistic effects of an electron for various kinetic energies.

Relativistic electron			
Kinetic energy E_k [eV]	Wavelength λ [m]	v/c [-]	m/m_0 [-]
10^0	1.22^{-09}	0.002	1.000002
10^1	3.86^{-10}	0.006	1.000020
10^2	1.22^{-10}	0.020	1.000196
10^3	3.86^{-11}	0.062	1.001957
10^4	1.22^{-11}	0.195	1.019567
$6 \cdot 10^4$	4.85^{-12}	0.446	1.117403
10^5	3.69^{-12}	0.548	1.195672
$3 \cdot 10^5$	1.96^{-12}	0.777	1.587016
10^6	8.69^{-13}	0.941	2.956719

Relativistic kinetic energy in the electric potential

The kinetic energy of charged particle with a relativistic velocity in the electrostatic potential Φ, [12] p. 19, is

$$e\Phi = \gamma mc^2 - mc^2. \tag{2.5}$$

Let's rewrite eq. (2.5) as

$$\frac{e\Phi}{mc^2} = \gamma - 1. \tag{2.6}$$

Let's define ε as

$$\varepsilon = \frac{e}{2mc^2} \tag{2.7}$$

and substitute eq. (2.7) to the eq. (2.5)

$$\gamma = 1 + 2\varepsilon\Phi, \tag{2.8}$$

$$\gamma^2 = (1 + 2\varepsilon\Phi)(1 + 2\varepsilon\Phi) = 1 + 4\varepsilon\Phi(1 + \varepsilon\Phi) = 1 + 4\varepsilon\Phi^*, \tag{2.9}$$

where Φ^* is so called relativistically corrected potential

$$\Phi^* = \Phi(1 + \varepsilon\Phi). \tag{2.10}$$

From Lorentz factor eq. (2.4) we get

$$v^2 = c^2\frac{\gamma^2 - 1}{\gamma^2} \tag{2.11}$$

and from eq. (2.9) we get eq. (2.7) and (2.11)

$$v^2 = c^2\frac{4\varepsilon\Phi^*}{\gamma^2} = \frac{1}{\gamma^2}\frac{2e\Phi^*}{m}. \tag{2.12}$$

The velocity of charged particle is

$$v = \frac{1}{\gamma}\sqrt{\frac{2e\Phi^*}{m}} = \frac{1}{1 + 2\varepsilon\Phi}\sqrt{\frac{2\varepsilon\Phi^*}{m}}. \tag{2.13}$$

For clarity let's define derivation notation with respect to the z coordination

$$\frac{dx}{dz} = x', \qquad \frac{dy}{dz} = y' \tag{2.14}$$

and with respect to the time t coordination

$$\frac{dx}{dt} = \dot{x}, \qquad \frac{dy}{dt} = \dot{y}, \qquad \frac{dz}{dt} = \dot{z}. \tag{2.15}$$

The magnitude of the velocity $\vec{v}$ in the Cartesian coordinate system x, y, z can be expressed as

$$\begin{aligned} v = |\vec{v}| &= \left[\left(\frac{dx}{dt}\right)^2 + \left(\frac{dy}{dt}\right)^2 + \left(\frac{dz}{dt}\right)^2\right]^{1/2} = \left[\left(\frac{dx}{dz}\frac{dz}{dt}\right)^2 + \left(\frac{dy}{dz}\frac{dz}{dt}\right)^2 + \left(\frac{dz}{dz}\frac{dz}{dt}\right)^2\right]^{1/2} = \\ &= \left[\left(\frac{dz}{dt}\right)^2 \cdot \left(\left(\frac{dx}{dz}\right)^2 + \left(\frac{dy}{dz}\right)^2 + 1\right)\right]^{1/2} = \frac{dz}{dt}\left(x'^2 + y'^2 + 1\right)^{1/2} = \\ &= \dot{z}\left(1 + x'^2 + y'^2\right)^{1/2} \qquad \text{for} \quad \dot{z} > 0, \end{aligned} \tag{2.16}$$

$$\dot{z} = \frac{v}{\left(1 + x'^2 + y'^2\right)^{1/2}}. \tag{2.17}$$

It helps us to calculate the velocity in z direction just from the magnitude of the velocity $\vec{v}$ and x' and y'. Keep in mind $\dot{z} > 0$ because it comes from the square root expression. The cross product of the velocity $\vec{v}$ and the magnetic induction $\vec{B}$ is

$$\vec{v} \times \vec{B} = \begin{pmatrix} \vec{i} & \vec{j} & \vec{k} \\ v_x & v_y & v_z \\ B_x & B_y & B_z \end{pmatrix} = \left(\dot{y}B_z - \dot{z}B_y, \dot{z}B_x - \dot{x}B_z, \dot{x}B_y - \dot{y}B_x\right). \tag{2.18}$$

So, the eq. (2.3) can be written by its components with help of eq. (2.19) for electron as

$$\begin{aligned} x : \frac{d}{dt}\left[\frac{m\dot{x}}{\sqrt{1-\frac{v^2}{c^2}}}\right] &= -e\left(E_x + yB_z - \dot{z}B_y\right), \\ y : \frac{d}{dt}\left[\frac{m\dot{y}}{\sqrt{1-\frac{v^2}{c^2}}}\right] &= -e\left(E_y + \dot{z}B_x - \dot{x}B_z\right), \\ z : \frac{d}{dt}\left[\frac{m\dot{z}}{\sqrt{1-\frac{v^2}{c^2}}}\right] &= -e\left(E_z + \dot{x}B_y - \dot{y}B_x\right). \end{aligned} \tag{2.19}$$

It is convenient to define complex variables

$$w(z) = x(z) + \mathrm{i}y(z), \tag{2.20}$$

$$E_w(z) = E_x(z) + \mathrm{i}E_y(z), \tag{2.21}$$

$$B_w(z) = B_x(z) + \mathrm{i}B_y(z). \tag{2.22}$$

So, by summing elements x and y from eq. (2.19) with substitution of eq. (2.20) and (2.21) we obtain

$$x + iy : \frac{d}{dt}[\gamma m\dot{w}] = -e\left(E_w - i\dot{w}B_z + i\dot{z}B_w\right) = -eE_w - ie\dot{z}\left(B_w - w'B_z\right) \tag{2.23}$$

and similarly for z

$$z : \frac{d}{dt}[\gamma m\dot{z}] = -e\left[E_z + \frac{1}{2i}\left(\dot{\bar{w}}B_w - \dot{w}\bar{B}_w\right)\right]. \tag{2.24}$$

The left side from eq. (2.23) with help of eq. (2.13) is

$$\begin{aligned} \frac{d}{dt}[\gamma m\dot{w}] = \frac{d}{dz}\frac{dz}{dt}[\gamma m\dot{w}] = \dot{z}\frac{d}{dz}[\gamma m w'\dot{z}] = \\ = \dot{z}\frac{d}{dz}\left[\frac{1}{\gamma}\left(\frac{2e\Phi^*}{m}\right)^{1/2}\frac{\gamma m w'}{\left(1 + w'\dot{w}'\right)^{1/2}}\right]. \end{aligned} \tag{2.25}$$

And we get the trajectory equation of electron in electric and magnetic field [13]

$$\frac{d}{dz}\left[\left(\frac{\Phi^*}{1+w'\bar{w}'}\right)^{1/2} w'\right] = -\frac{1}{2}E_w\gamma\left(\frac{1+w'\bar{w}'}{\Phi^*}\right)^{1/2} - i\eta\left(B_w - w'B_z\right), \tag{2.26}$$

only for electron $e > 0$ and for $v_z > 0$, where η is

$$\eta = \sqrt{\frac{e}{2m}}. \tag{2.27}$$

2.3. Paraxial approximation

If the electron moves close to the optical axis, its trajectory can expressed from eq. (2.26) in the form of the paraxial equation for rotationally symmetric fields

$$w'' + \left(\frac{\gamma\Phi'}{2\Phi^*} - \frac{i\eta}{\sqrt{\Phi^*}}B\right)w' + \left(\frac{\gamma\Phi''}{4\Phi^*} - \frac{i\eta}{2\sqrt{\Phi^*}}B'\right)w = 0, \tag{2.28}$$

where $\Phi = \Phi(z)$ is the electrostatic potential define as $\vec{E} = -\nabla\Phi$ and $B = B(z)$ the magnetic induction on the optical axis in the paraxial approximation [13].

2.4. General expansion of magnetic field

A magnetic field in the paraxial domain is of the utmost importance in electron optics. In the proximity of the optical axis, the magnetic field can be expressed as a radial series expansions only from the axial reduced magnetic potential ψ_m. So, only from the knowledge of reduced magnetic potential on the optical axis the magnetic field can be derived. It is assumed that the optical axis is straight and the paraxial domain is source free, i.e., all windings of coils are far away from the optical axis [12] p. 73.

The magnetic scalar potential Ψ can be expressed from the Laplace equation [13] as

$$\Psi(r,\varphi,z) = \sum_{m=0}^{\infty}\sum_{i=0}^{\infty}(-1)^i\frac{1}{4^i}\frac{m!}{i!(m+i)!}\psi_m^{(2i)}(z)r^{2i+m}\cos(m\varphi+\alpha_m) \tag{2.29}$$

where ψ_m is the axial reduced magnetic potential, r is radial distance and α_m is angle of rotation.

The magnetic induction in cylindrical coordinates is

$$\vec{B} = -\mu_0\nabla\Psi = -\mu_0\Big(\frac{\partial\Psi}{\partial r}, \frac{1}{r}\frac{\partial\Psi}{\partial\varphi}, \frac{\partial\Psi}{\partial z}\Big), \tag{2.30}$$

so the equation (2.29) becomes

$$B_r = -\mu_0\sum_{m=0}^{\infty}\sum_{i=0}^{\infty}(-1)^i\frac{2i+m}{4^i}\frac{m!}{i!(m+i)!}\psi_m^{(2i)}(z)r^{2i+m-1}\cos(m\varphi+\alpha_m), \tag{2.31}$$

$$B_\varphi = \mu_0\sum_{m=0}^{\infty}\sum_{i=0}^{\infty}(-1)^i\frac{m}{4^i}\frac{m!}{i!(m+i)!}\psi_m^{(2i)}(z)r^{2i+m-1}\sin(m\varphi+\alpha_m), \tag{2.32}$$

$$B_z = -\mu_0\sum_{m=0}^{\infty}\sum_{i=0}^{\infty}(-1)^i\frac{1}{4^i}\frac{m!}{i!(m+i)!}\psi_m^{(2i+1)}(z)r^{2i+m}\cos(m\varphi+\alpha_m). \tag{2.33}$$

Rotationally symmetric fields

Rotationally symmetric fields are important for description of magnetic lenses. They do not depend on the angle φ. The magnetic scalar potential Ψ_0 and magnetic induction $\vec{B_0}$ is obtain from (2.29) and (2.30) for conditions $\alpha_0 = 0$ and $m = 0$ as

$$\Psi_0(r,\varphi,z) = \sum_{i=0}^{\infty}(-1)^i \frac{1}{4^i}\frac{1}{(i!)^2}\psi_0^{(2i)}(z)r^{2i}, \tag{2.34}$$

$$B_{r,0} = -\mu_0 \sum_{i=0}^{\infty}(-1)^i \frac{2i}{4^i}\frac{1}{(i!)^2}\psi_0^{(2i)}(z)r^{2i-1}, \tag{2.35}$$

$$B_{\varphi,0} = 0, \tag{2.36}$$

$$B_{z,0} = -\mu_0 \sum_{i=0}^{\infty}(-1)^i \frac{1}{4^i}\frac{1}{(i!)^2}\psi_0^{(2i+1)}(z)r^{2i}. \tag{2.37}$$

Dipole field

The dipole field is important for description of deflection coils and contrary to the magnetic lenses it does depend on the angle φ. The magnetic scalar potential Ψ_1 and the magnetic induction $\vec{B_1}$ is obtain from (2.29) and (2.30) for condition $m = 1$ as

$$\Psi_1(r,\varphi,z) = \sum_{i=0}^{\infty}(-1)^i \frac{1}{4^i}\frac{1}{i!(1+i)!}\psi_1^{(2i)}(z)r^{2i+1}\cos(\varphi+\alpha_1), \tag{2.38}$$

$$B_{r,1} = -\mu_0 \sum_{i=0}^{\infty}(-1)^i \frac{2i+1}{4^i}\frac{1}{i!(1+i)!}\psi_1^{(2i)}(z)r^{2i}\cos(\varphi+\alpha_1), \tag{2.39}$$

$$B_{\varphi,1} = \mu_0 \sum_{i=0}^{\infty}(-1)^i \frac{1}{4^i}\frac{1}{i!(1+i)!}\psi_1^{(2i)}(z)r^{2i}\sin(\varphi+\alpha_1), \tag{2.40}$$

$$B_{z,1} = -\mu_0 \sum_{i=0}^{\infty}(-1)^i \frac{1}{4^i}\frac{1}{i!(1+i)!}\psi_1^{(2i+1)}(z)r^{2i+1}\cos(\varphi+\alpha_1). \tag{2.41}$$

Quadrupole field

The quadrupole field is crucial for description of stigmators. The magnetic scalar potential Ψ_2 and magnetic induction $\vec{B_2}$ is obtain from (2.29) and (2.30) for condition $m = 2$ as

$$\Psi(r,\varphi,z) = \sum_{i=0}^{\infty}(-1)^i \frac{1}{4^i}\frac{2}{i!(2+i)!}\psi_2^{(2i)}(z)r^{2i+2}\cos(2\varphi+\alpha_2) \tag{2.42}$$

$$B_{r,2} = -\mu_0 \sum_{i=0}^{\infty}(-1)^i \frac{2i+2}{4^i}\frac{2}{i!(2+i)!}\psi_2^{(2i)}(z)r^{2i+1}\cos(2\varphi+\alpha_2) \tag{2.43}$$

$$B_{\varphi,2} = \mu_0 \sum_{i=0}^{\infty}(-1)^i \frac{2}{4^i}\frac{2}{i!(2+i)!}\psi_2^{(2i)}(z)r^{2i+1}\sin(2\varphi+\alpha_2) \tag{2.44}$$

$$B_{z,2} = -\mu_0 \sum_{i=0}^{\infty} (-1)^i \frac{1}{4^i} \frac{2}{i!(2+i)!} \psi_2^{(2i+1)}(z) r^{2i+2} \cos(2\varphi + \alpha_2). \tag{2.45}$$

The power series can be found in the book Electron optics by Peter W. Hawkes, and Erwin Kasper [14] on pages 87-89.

2.5. Deflection of electron beam

Every kind of electron beam technology utilizes a deflection to a greater or lesser degree. To achieve deflection of the electron beam, either transverse electrostatic or magnetic fields is applied. The main focus is to achieve a lateral shift of the focused electron beam spot (the electron probe) with as little disturbance as possible. The focused spot is moved in a raster pattern over a specified area of a specimen or a screen. Prominent examples are various electron and ion microscopes, electron lithographs, focused ion beam technology, oscilloscope cathode-ray tubes, and television tubes. Furthermore, even instruments with a fixed beam, such as transmission electron microscope, use the deflection for non-mechanical alignment of the column. It is also necessary to use a deflection system for electron-beam blanking. An exciting application is a scanning electron microscope, where magnification is altered just by changing the scanned area of the sample. However, high resolution is connected with small deflection angles and proximity of the pole pieces to the sample (working distance) to minimize spherical and chromatic aberrations. For such applications, the design of the deflection system is as essential as the design of the lenses [14] p. 483-483.

2.5.1. Simplified deflection of electrons by constant field

Electrons accelerated by voltage U with the kinetic energy $E = eU$ pass trough a uniform electric field of a parallel-plate capacitor $|\vec{E}| = u/d$, where $\pm u/2$ is the bias and d is distance between two plates, or trough a uniform magnetic field $|\vec{B}|$, see Fig. 2.1. For small angles of deflection γ is used $\gamma = x/L$ because of $\sin\gamma \simeq \tan\gamma \simeq \gamma$. So, electrons pass trough the uniform transverse fields of length h and they have a constant momentum component $p_z = mv$. Then Lorentz force $\vec{F} = \mathrm{d}\vec{p}/\mathrm{d}t$ acts on electrons and changes its momentum component p_x during the time $T = h/v$ as

$$p_x = \int_0^T F_x \,\mathrm{d}t = e \int_0^T (E_x + vB_y)\,\mathrm{d}t = \frac{e}{v} \int_0^h (E_x + vB_y)\,\mathrm{d}z = eh\,(E_x/v + B_y)\,. \tag{2.46}$$

The angle of deflection is than $\gamma = |p_x|\,/p_z$ and by using relativistic momentum as

$$p = mv = \left[2m_0 E\,(1 + E/2E_0)\right]^{1/2}. \tag{2.47}$$

we receive for deflection by electric field

$$\gamma = \frac{eh}{mv^2} E_x = \frac{h}{2d} \frac{u}{U} \frac{1 + E/E_0}{1 + E/2E_0} \tag{2.48}$$

and for deflection by electric field

$$\gamma = \frac{eh}{mv} B_y = \frac{ehB_y}{\left[2m_0 E\,(1 + E/2E_0)\right]^{1/2}}, \tag{2.49}$$

where $E_0 = m_0c^2$. This approach is introduced by Ludwig Reimer in [12] p. 39.

Notice that the angle of magnetic deflection is inversely proportional to the square root of the electron accelerating voltage. However, the angle in electrostatic deflection is inversely proportional to the electron accelerating voltage. So, magnetic deflection is preferred for high energies of particles. Moreover, magnetic deflectors can be used without significantly increasing current for higher accelerating voltages difference. Electrostatic deflectors need a high voltage supply, they take up more space, and they are limited by the dielectric strength of the vacuum, around 3 kV/mm. Additionally, two capacitor plates work like an ion vacuum pump, which causes additional noise. Nevertheless, electrostatic deflectors are standard for oscilloscope displays because it is easier to scan at high frequencies. Scanning with magnetic deflectors at high frequencies is limited by the large inductance of the deflection coils.

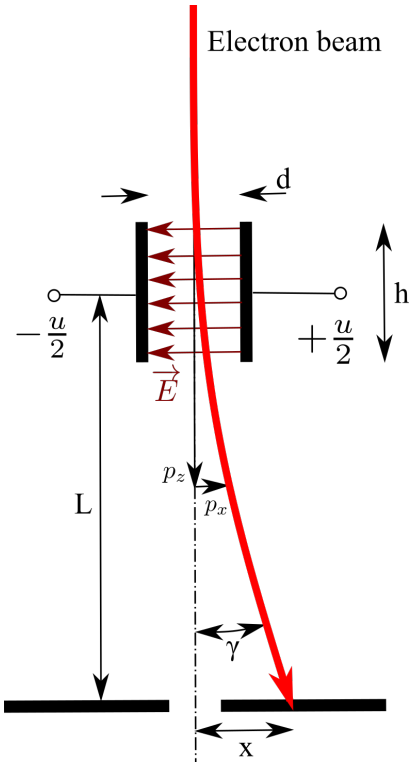

Fig. 2.1: Deflection of the electron beam by electrostatic deflector. Adapted from [12] p. 39.

2.6. Transmission electron microscope design

The TEM design can vary wildly depending on abilities (Scanning TEM, Low-voltage electron microscope, Cryo-TEM, Environmental TEM, Aberration corrected TEM, and Ultrafast and dynamic TEM) and manufacturer. The main components are summed up below, and in Fig. 2.2 [15] p. 9.

- **Electron source**: It is a electrical device that creates a electron beam in the vacuum. It is very important that the electron gun produce a very narrow electron beam (high brightness) with a small difference in kinetic energy from 0.2 eV to 3 eV to limit chromatic aberration. There are four main types of electron beam emission

mechanisms: thermionic emission, Schottky effect field emission gun, field electron emission, and photocathode.

- **Accelerator**: One or more anodes that accelerate electrons to the required energy. The typical kinetic energy of the electron is from 60 keV to 300 keV nowadays.
- **Electron lens**: Is used an electric or magnetic field to focus an electron beam by use of Lorentz force. The typical optical system uses several condenser lenses, objective lenses, and projective lenses to focus the electron beam from the source to the sample and then the image sample to the detector.
- **Apertures**: They are used to limit the diameter of the electron beam to suppress the impact of optical aberrations as well as to lower the number of stray electrons to decrease noise. However, too small apertures decrees electron current and limit resolution because of the diffraction limit.
- **Stigmators**: They are used to correct optical aberration called astigmatism. Their coils create quadrupole, hexapole, octupole, and higher magnetic fields, and they create a much weaker field than magnetic lenses. Several stigmators are commonly used at multiple positions to correct electron beam.
- **Specimen region**: A vacuum chamber where the sample where is located. The sample is inserted via airlocks to mitigate vacuum deterioration inside of TEM. The pressure around the sample is commonly better than 10^{-4} Pa, but more specialized microscopes can reach the specimen region pressure up to 10^{2} Pa as it is in the case of environmental TEM.
- **Specimen holder**: A mechanism, which holds the sample during a transport and measurement. Movement is utilized in the x and y direction up to ± 1 mm and up to ± 0.5 mm in the z-direction. For tomography measurement, it is possible to tilt the sample up to $\pm 70°$. More advanced TEM utilizes heating or cooling of the sample. A great afford focused on limiting the thermal shift of the sample during measurement.
- **Vacuum system**: Sufficient vacuum level has to be reached in order to increase the mean free path of the electrons. A high vacuum level is also required for various working principles of the electron gun. Air is pumped with the help of vacuum pumps in several stages because there is no vacuum pump that can effectively work from the atmospheric pressure up to ultra-high vacuum. The first stage usually consists of a rotary vane pump or diaphragm pump. In the next stage, the turbomolecular or diffusion pump reaches HV. For reaching UHV conditions, an ion pump or a sorption pump is used.
- **Detectors**: The primary electrons of the electron beam interact with the sample. The interaction produces elastic and non-elastic scattered electrons, secondary electrons, cathodoluminescence, or X-rays. Commonly used detectors are X-ray detectors, CCD and CMOS cameras, fluorescent viewing screens, or electron energy loss spectrometers.

- **Lens power supply**: An indispensable part of the TEM design is very stable current and voltage sources. The typical stability of the source is 10 ppm or better.
- **Personal computer**: Since the design of Tecnai TEM in 1998, the trend has been to operate TEM with the remote control of the operator, and more and more processes are being automated and controlled via personal computer. These benefits lower acoustic vibration and thermal expansion caused by human presence.

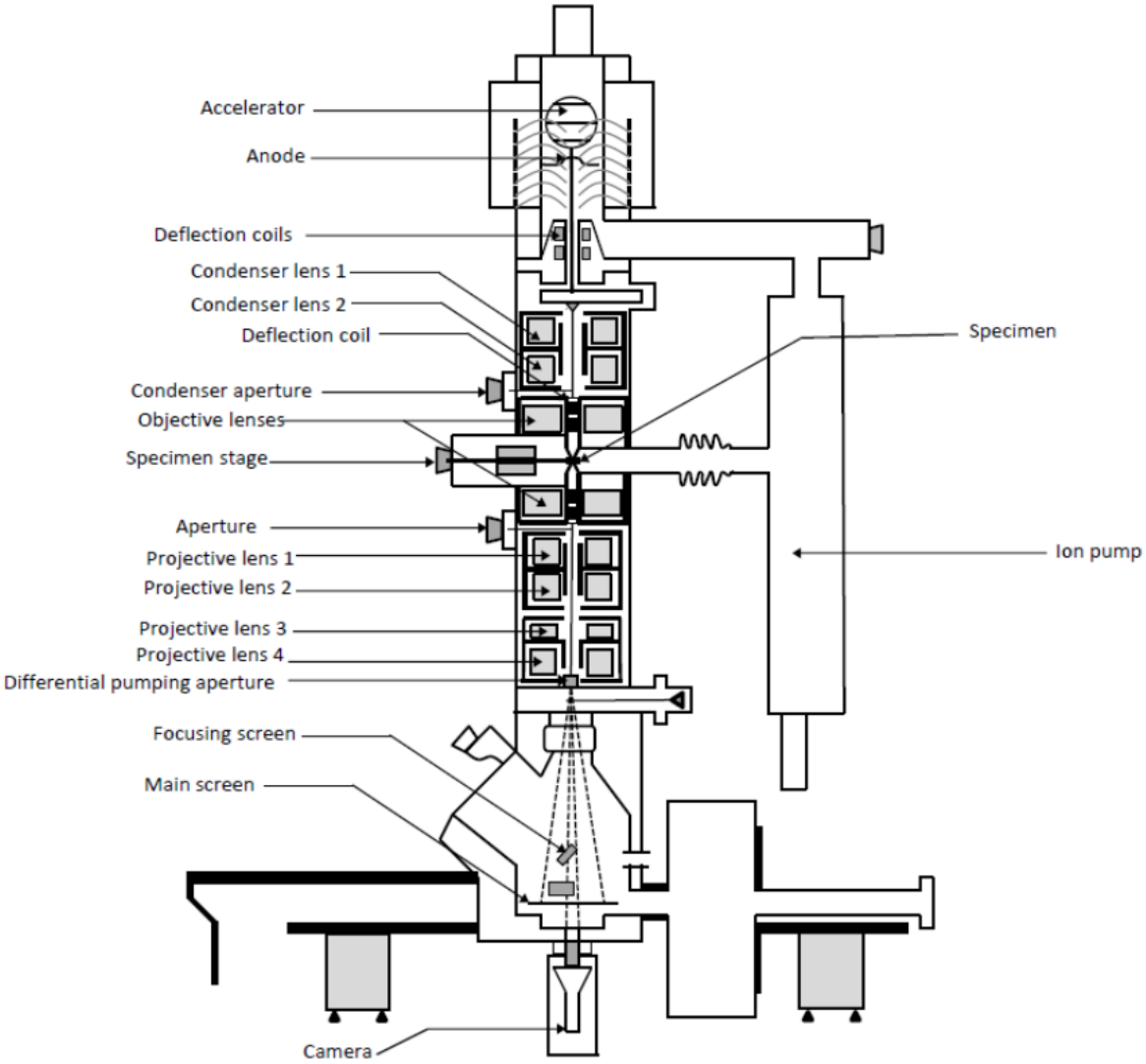

Fig. 2.2: The design of the transition electron microscope and its main components [15] p. 10.

2.7. Correction elements

"Like much else in real life, electron-optical systems are not perfect" - *Handbook of Charged Particle Optics* [12] p. 601.

Literature distinguishes *fundamental aberrations* and *parasitic aberrations*. The spherical aberration of perfectly round lenses represents fundamental aberrations. Misaligned objectives lenses, magnetic inhomogeneities of the polepieces, thermal drift, misshaped

polepieces, and misaligned deflectors or departure from rotational symmetry during machining in general causes astigmatism as well. They collectively represent parasitic aberrations. Various devices are deployed for the correction of optical aberration of electron-optical systems. These devices include deflectors, stigmators, electrostatic mirrors, and spherical and chromatic aberration correctors. [23] p. 601

2.7.1. Deflectors

Deflectors create a dipole electric or magnetic field to deflect charged particles. It is crucial to position the sample close to the lens to keep the aberration influence low. Hence, the deflectors are positioned upstream from the lens. An important application for magnetic deflection coils is TEM to fine adjust the concentricity of electron-optical elements. During the production and assembly of the microscope parts, the inevitable mechanical misalignment of the optical elements occurs. This occurs not only due to limited production accuracy but also due to the limited assembly accuracy of mechanical parts. So, it is impossible to reach the required production precision for the concentricity of elements by mechanical means. When an electron beam propagates from one optical element to another, the coaxiality of the optical elements must be maintained, see Fig. 2.3 (a). This axial misalignment causes the electron beam to propagate asymmetrically off the optical axis. Therefore, higher aberrations are observed. Nevertheless, manufacturers found a solution in the form of magnetic deflectors. Pair of the magnetic deflector in X and Y is placed between each optical element to maintain concentricity, see Fig. 2.3 (b). Thus, mechanical imperfections are compensated, and optical aberrations are greatly reduced cost-effectively. It is necessary to manufacture the deflection coils with high accuracy. To deflect the electron beam in both X and Y direction, a set of two deflectors is used and they are rotated 90° to each other. Magnetic deflectors are more commonly used due to their stronger deflection force for electrons and lower aberrations. The most wildly used magnetic defectors are summarized below.

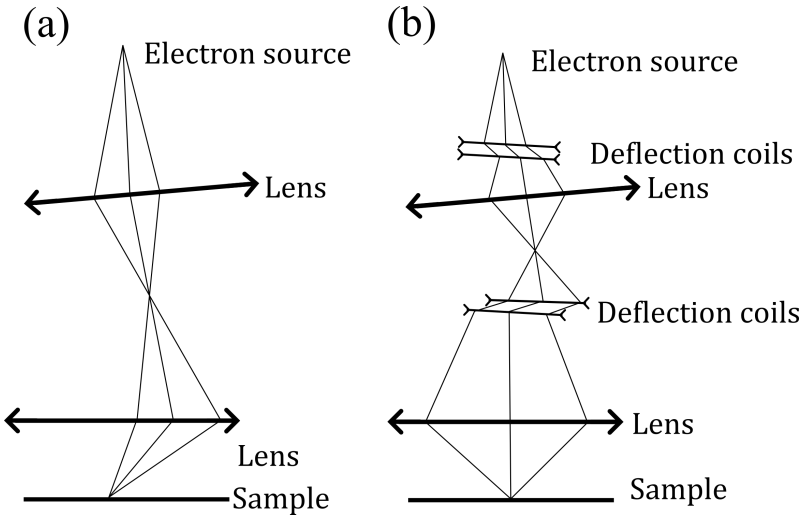

Fig. 2.3: An optical system is suffering from the inevitable mechanical misalignment in (a). The corrected optical system by sets of deflection coils in (b).

Toroidal deflectors

The toroidal deflector consists of four coils and its wires are wounded in the plane, see Fig. 2.4. Wires are wound on the rotationally symmetric magnetic form with respect to the Z axis, and wires also lie in a plane together with the Z axis. The magnetic form with coils has to be placed with respect to the optical axis of lenses. Wires supplying current to the coils are supposed not to contribute to the deflection field by its magnetic field. Otherwise, the quality of performance is worsened by additional aberrations due to misalignment and inaccuracy of placement. All these factors make the manufacturing process more challenging and expensive [14] p. 483-484.

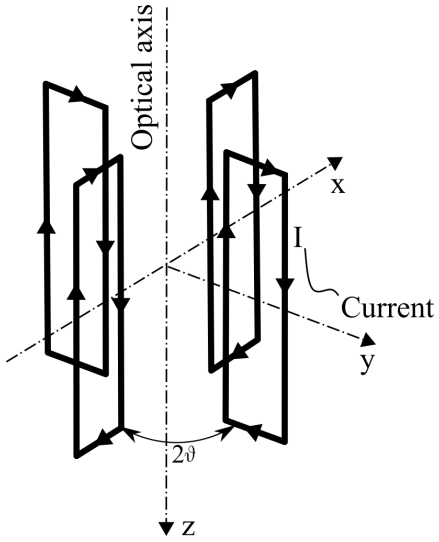

Fig. 2.4: Toroidal deflector for one direction. It consists of four coils and opposite coils lie in a plane. The half-angle is $\vartheta = \pi/3$ rad.

Helmholtz coil deflectors

A Helmholtz coil is a device that produces a region with an almost uniform magnetic field, i.e., $\partial^2 B/\partial z^2 = 0$. It is named after the German physicist Hermann von Helmholtz. It consists of two identical circular coils (electromagnets) connected in series (both coils carry an equal electric current I), and they are placed coaxially, Fig. 2.5. They both have an equal amount of turns N, the radius R, and the distance between two coils is also R to create as much homogeneous magnetic field between the coils as possible. Helmholtz coil is a wildly used instrument to cancel the Earth's magnetic field or other external magnetic fields. The magnetic induction in the middle of two coils is given by [16]

$$B = \left(\frac{4}{5}\right)^{3/2} \frac{\mu_0 N I}{R}, \tag{2.50}$$

where μ_0 is the vacuum permeability. An exciting application of this coil is in the form of a double-focusing Helmholtz-coil spectrometer. It is a core-free spectrometer under development with an expected momentum resolution of 0.3% [17]. Helmholtz coil deflectors are considered to be a subset of general saddle coil deflectors. In today's TEM, Helmholtz coils are not used due to higher optical aberrations than the saddle coils.

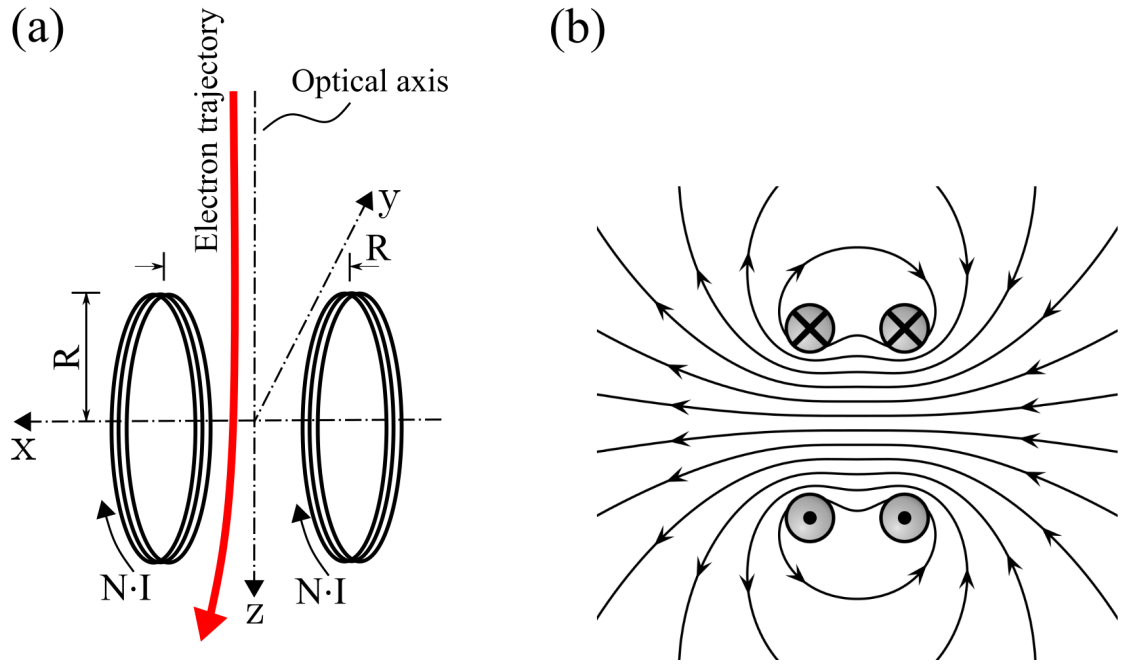

Fig. 2.5: (a): Helmholtz-coil diagram with a deflected electron beam. Flowing current creates magnetic induction in the $+X$ direction. Hence, the electron beam is deflected in $-$ (b): Cross-section of the Helmholtz coil with magnetic field lines. Note that the magnetic field is almost uniform [19].

Saddle coil deflectors

Saddle-shaped coils are convenient for generating a magnetic field perpendicular to the optical axis Z, see Fig 2.6. It consists of two identical coils which are bent on the cylinder. Each part carries the same current I, and the current flows in the same direction in the Z axis [14] p. 483-487. The current generates a magnetic induction at the origin in the X direction. Such magnetic induction deflects the electron beam in the $+Y$ direction. It is crucial to design the saddle coil with optimum geometry. The saddle coil is almost always designed with the full angle $2\vartheta = 120°$ to nullify the hexapole field, which is responsible for three-fold astigmatism. The problem of maximizing the uniformity of the magnetic field around the origin was studied as well, and it was found to be $2\vartheta = 120°$ and $h/D = 2$ [18]. The drawing with the dimensions of the saddle coil and with the core is in Fig. 2.7.

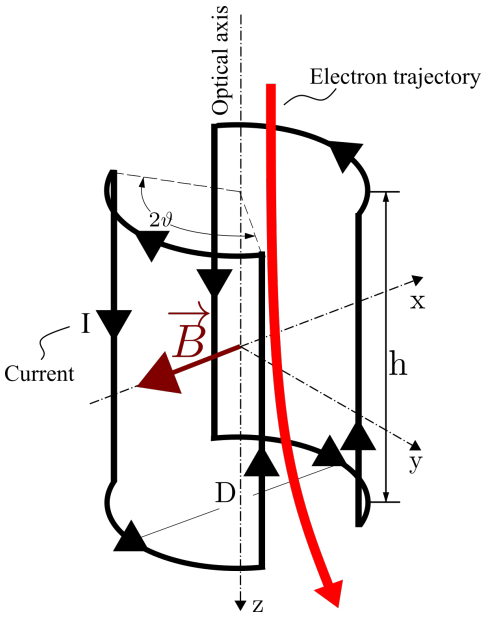

Fig. 2.6: The geometry of the saddle deflection coil with the full angle 2ϑ, height h, diameter D and current I.

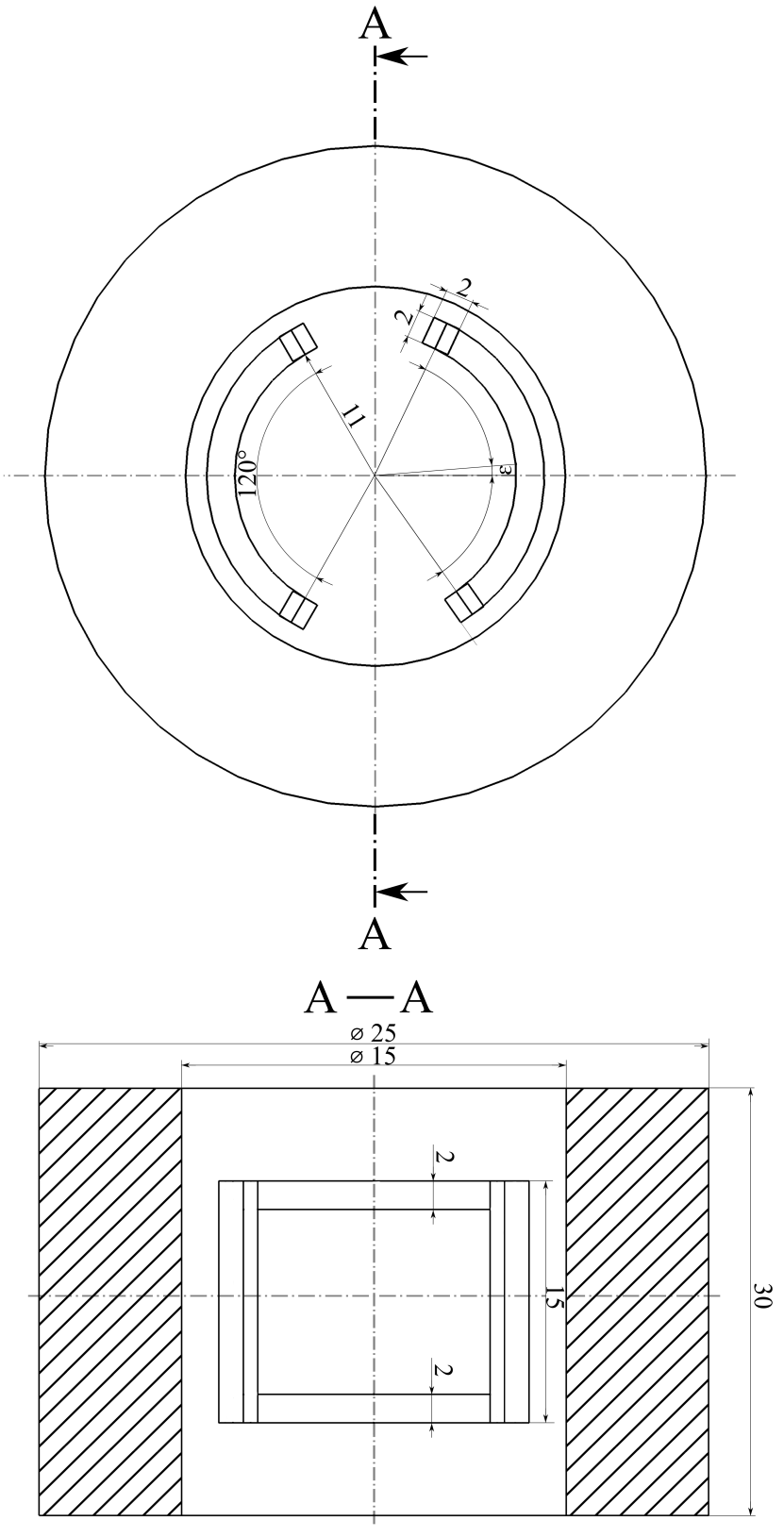

Fig. 2.7: Design of the saddle coil with its dimensions and ferrite core made of iron. This design is used for simulation in EOD and COMSOL software to study the effect of misalignment ε. Simulated for 10 Ampere-turns, $h = 15$ mm, $D = 2R = 22$ mm and $\vartheta = \pi/3$ rad.

2.7.2. Stigmators

A stigmator is a device of electron microscopes for the correction of optical aberration called astigmatism. Astigmatism limits the resolution of electron microscope [12] p. 32. Therefore, almost all current electron microscopes correct astigmatism with stigmators to improve the resolution. Depending on the number of electrodes, it creates an electrostatic or magnetic quadrupole, hexapole, or octupole. The quadrupole stigmator creates a quadrupole field perpendicular to the electron beam to reshape the elliptic cross-section of the beam to the circular cross-section, see Fig 2.8. Thus, 2-fold astigmatism is corrected [14] p. 859. The stigmators field is much weaker compared to the field of lenses. Only one stigmator pair is usually used in the SEM, but TEM designs commonly use several stigmator pairs.

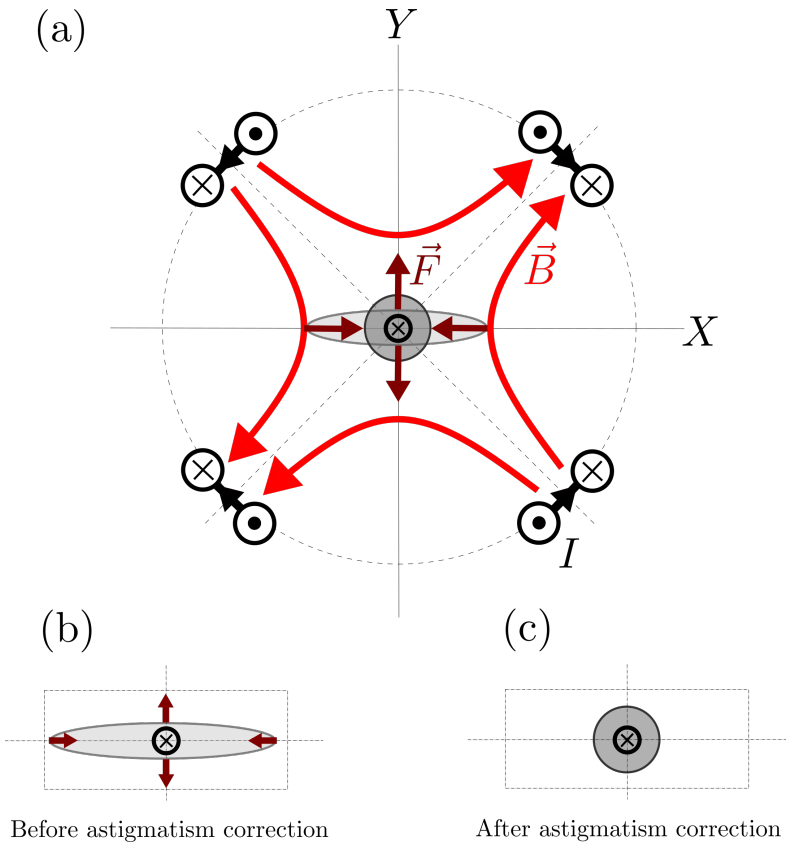

Fig. 2.8: (a): An axial view of a quadrupole stigmator for correction of twofold astigmatism. Electric current I flows through a set of coils to generate a magnetic quadrupole. Magnetic induction $\vec{B}$ acts on the electron beam, and the Lorenz force $\vec{F}$ reshapes the electron beam from an elliptical shape to a circular shape. Therefore, astigmatism is corrected. (b): Before astigmatism correction. (C): After astigmatism correction.

3. Calculation methods

Novel methods for calculating multipole fields of the misaligned saddle coil are introduced in this chapter. The most recent version 5.009 of EOD (Electron optical design) software [21] does not include an option for calculating multipole fields of the misaligned saddle coil, a misaligned multipole in general. Thus, the main effort is focused on developing mathematical methods that could calculate the multipole fields of the misaligned saddle coil and be implemented in the EOD software as well. The three new methods are the infinite dipole method, the normalized Fourier series coefficients method and the corrected multipole method. These new methods are then compared with results obtained by the 3D finite element method (3D FEM) COMSOL Multiphysics [22] to validate the new methods independently. The main advantage is in the saving of computational time. The computation time for the standard saddle coil is in the order of 10^0 s for EOD. The standard computation time for the competitive method 3D FEM is 10^0 h for COMSOL Multiphysics. So, time savings during an electron-optic development could be enormous.

3.1. The infinite dipole method

Novel method* for calculation of the magnetic scalar potential $\Psi(\varphi, r)$ of the misaligned, infinitely long saddle coil is introduced in this section. The idea of this approach is sometimes called the top-hat method, because the field of the infinite coil is then reduced to the height h to approximate the real-size deflection coil. This method can be used for fast approximation of multipoles fields due to the misalignment. The magnetic scalar potential for an infinitely long dipole, see Fig. 3.1, can be described as

$$\Psi(\varphi, r) = \sum_{m=0}^{\infty} \psi_{a,m} \left(\frac{r}{R}\right)^m \cos(m\varphi) + \sum_{m=0}^{\infty} \psi_{b,m} \left(\frac{r}{R}\right)^m \sin(m\varphi) \tag{3.1}$$

where r is a radial distance from the optical axis to the windings and radius R, $\psi_{a,m}$ is a reduced axial magnetic multipole potential for multipole of order m of radius R

$$\psi_{a,m} = \frac{\mu_0 M}{2\pi R^m} \int_a^b \cos(m\varphi) NI f_\varepsilon(\varphi) d\varphi, \tag{3.2}$$

where μ_0 is permeability of vacuum. If the coil is surrounded by magnetic material of radius R_{mat}, the coefficient is $M = 1 + (1 + R/R_{mat})^{2m}$. $f_\varepsilon(\varphi)$ is azimuthal unit current distribution of the misaligned saddle coil, see eq. (3.14), NI stands for number of ampere-turns of the coil. Similarly, the $\psi_{b,m}$ is a magnetic scalar potential for multipole of order m

$$\psi_{b,m} = \frac{\mu_0 M}{2\pi R^m} \int_a^b \sin(m\varphi) NI f_\varepsilon(\varphi) d\varphi. \tag{3.3}$$

$\psi_{a,m}$ and $\psi_{b,m}$ enable us to determinate all reduced axial field functions of the misaligned saddle coil. The infinite dipole method is only approximation to the finite dipole.

*Method proposed by Dr. Peter Tiemeijer and Dr. Ondřej Sháněl.

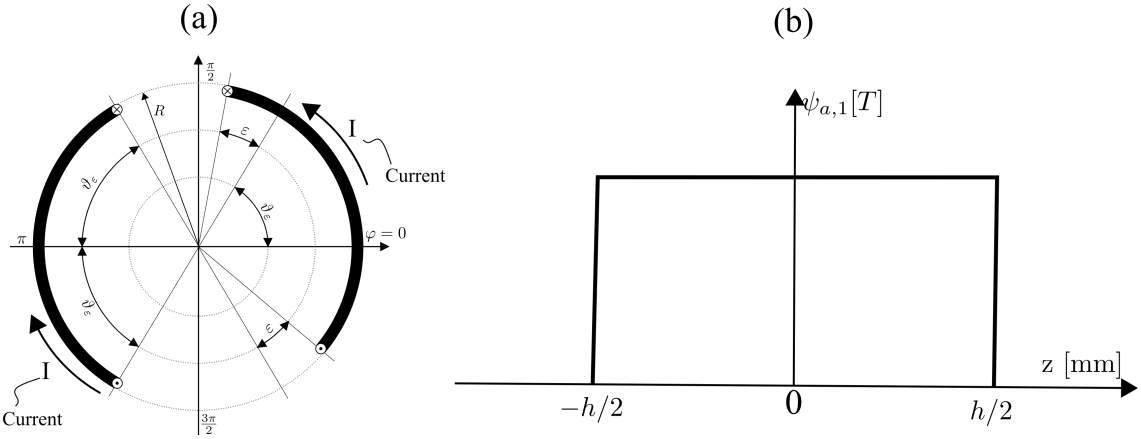

Fig. 3.1: (a): An axial view of the saddle deflection coil with half-angle $\vartheta_\varepsilon = \pi/3$ rad with the angle of misalignment ε and radius R. (b): Axial reduced dipole magnetic potential $\psi_{a,1}$ of the deflection coil of height h for the infinite dipole method. It is an approximation according to the top-hat method.

The magnetic scalar multipole potentials are thus calculated for the angle of misalignment ε of the saddle coil and the coil winding half-angle $\vartheta_\varepsilon = \pi/3$ rad as

$$\psi_{a,m} = \frac{\mu_0 M}{2\pi R^m}\left[\int_{-\frac{\pi}{3}+\varepsilon}^{\frac{\pi}{3}+\varepsilon} NI\cos(m\varphi)d\varphi - \int_{\frac{2\pi}{3}}^{\frac{4\pi}{3}} NI\cos(m\varphi)d\varphi\right]. \tag{3.4}$$

$$\psi_{a,m} = \frac{\mu_0 NIM}{m\pi R^m}\left\{\Big[\sin m\varphi\Big]_{-\frac{\pi}{3}+\varepsilon}^{\frac{\pi}{3}+\varepsilon} - \Big[\sin m\varphi\Big]_{\frac{4\pi}{3}}^{\frac{2\pi}{3}}\right\}, \tag{3.5}$$

$$\psi_{a,m} = \frac{\mu_0 NIM}{m\pi R^m}\left\{ -2\sin\frac{m\left(+\frac{\pi}{3}+\varepsilon+\frac{\pi}{3}-\varepsilon\right)}{2}\sin\frac{m\left(-\frac{\pi}{3}+\varepsilon-\frac{\pi}{3}-\varepsilon\right)}{2} - 2\sin\frac{m\pi\frac{4-2}{3}}{2}\sin\frac{m\pi\frac{4+2}{3}}{2}\right\},$$

$$\psi_{a,m} = \frac{\mu_0 NIM}{m\pi R^m}\left[\sin\frac{m\pi}{3}\cos m\varepsilon - \sin\frac{m\pi}{3}\cos m\pi\right], \tag{3.6}$$

$$\psi_{a,m} = \frac{\mu_0 NIM}{m\pi R^m}\sin\frac{m\pi}{3}\Big[\cos(m\varepsilon) - \cos(m\pi)\Big]. \tag{3.7}$$

Similarly, the $C_{b,m}$ is calculated

$$\psi_{b,m} = \frac{\mu_0 M}{2\pi R^m}\left[\int_{-\frac{\pi}{3}+\varepsilon}^{\frac{\pi}{3}+\varepsilon} NI\sin(m\varphi)d\varphi - \int_{\frac{2\pi}{3}}^{\frac{4\pi}{3}} NI\sin(m\varphi)d\varphi\right], \tag{3.8}$$

$$\psi_{b,m} = -\frac{\mu_0 NIM}{2n\pi R^m}\left\{\Big[\cos m\varphi\Big]_{-\frac{\pi}{3}+\varepsilon}^{\frac{\pi}{3}+\varepsilon} - \Big[\cos m\varphi\Big]_{\frac{4\pi}{3}}^{\frac{2\pi}{3}}\right\}, \tag{3.9}$$

$$\psi_{b,m} = \frac{\mu_0 NIM}{2n\pi R^m}\left\{\Big[\cos m\varphi\Big]_{\frac{\pi}{3}+\varepsilon}^{-\frac{\pi}{3}+\varepsilon} - \Big[\cos m\varphi\Big]_{\frac{2\pi}{3}}^{\frac{4\pi}{3}}\right\}, \tag{3.10}$$

$$\psi_{b,m} = \frac{\mu_0 NIM}{2m\pi R^m}\left\{ \cos\left(m\Big(-\frac{\pi}{3}+\varepsilon\Big)\right) - \cos\left(m\Big(\frac{\pi}{3}+\varepsilon\Big)\right) + \cos\left(m\frac{4\pi}{3}\right) - \cos\left(m\frac{2\pi}{3}\right)\right\}, \tag{3.11}$$

$$\psi_{b,m} = \frac{\mu_0 NIM}{2m\pi R^m}\left\{ -2\sin\frac{m\left(-\frac{\pi}{3}+\varepsilon+\frac{\pi}{3}+\varepsilon\right)}{2}\sin\frac{m\left(-\frac{\pi}{3}+\varepsilon-\frac{\pi}{3}-\varepsilon\right)}{2} \right.$$
$$\left. -2\sin\frac{m\pi\frac{4+2}{3}}{2}\sin\frac{m\pi\frac{4-2}{3}}{2}\right\},$$

$$\psi_{b,m} = \frac{\mu_0 NIM}{2m\pi R^m}\left\{-2\sin(m\varepsilon)\sin\left(-m\frac{\pi}{3}\right) - 2\sin(m\pi)\sin\left(m\frac{\pi}{3}\right)\right\}, \tag{3.12}$$

$$\psi_{b,m} = \frac{\mu_0 NIM}{m\pi R^m}\sin\frac{m\pi}{3}\sin(m\varepsilon). \tag{3.13}$$

3.2. The normalized Fourier series coefficients method

Newly developed normalized Fourier series coefficients method enables us to calculate all reduced axial magnetic multipole potential functions for the misaligned saddle coil. The problem of the misaligned deflection coil is reduced to the sum of fields of perfect multipole, for which there are already known solutions. The normalized Fourier series coefficients method consists of calculation of the Fourier series coefficients of current unit I of the angular distribution of the excitation for the asymmetrical saddle coil, see Fig. 3.2 (b). The normalization of the Fourier series coefficients has to be carried out as well. Normalized Fourier series coefficients are used to find out the correct value for all reduced axial magnetic multipole potential functions for misaligned saddle coil. The method for analytical and numerical computation of multipole components of a perfectly aligned saddle coil is published by prof. Lencová in [20]. This method is implemented in the EOD [21] software and is used to calculate axial field functions of perfect general multipole $\psi_{m,p}$ for Normalized Fourier series coefficients method. Therefore, the misaligned deflection coil problem is reduced on the group of previously solved problems.

Let us define an angular distribution of the unit excitation for the saddle coil $f_\varepsilon(\varphi)$ with the half-angle ϑ_ε and the angle of misalignment ε on the interval $[0, 2\pi]$ as follow

$$f_\varepsilon(\varphi) = \begin{cases} 1 & \varphi \in [0, \vartheta_\varepsilon + \varepsilon)\,, \\ 0 & \varphi \in [\vartheta_\varepsilon + \varepsilon, \pi - \vartheta_\varepsilon)\,, \\ -1 & \varphi \in [\pi - \vartheta_\varepsilon, \pi + \vartheta_\varepsilon)\,, \\ 0 & \varphi \in [\pi + \vartheta_\varepsilon, 2\pi - \vartheta_\varepsilon + \varepsilon)\,, \\ 1 & \varphi \in [2\pi - \vartheta_\varepsilon + \varepsilon, 2\pi]\,. \end{cases} \tag{3.14}$$

The positive $+1$ and negative -1 value denotes direction of unit current flow in Fig. 3.2 (b) and Fig. 3.3.

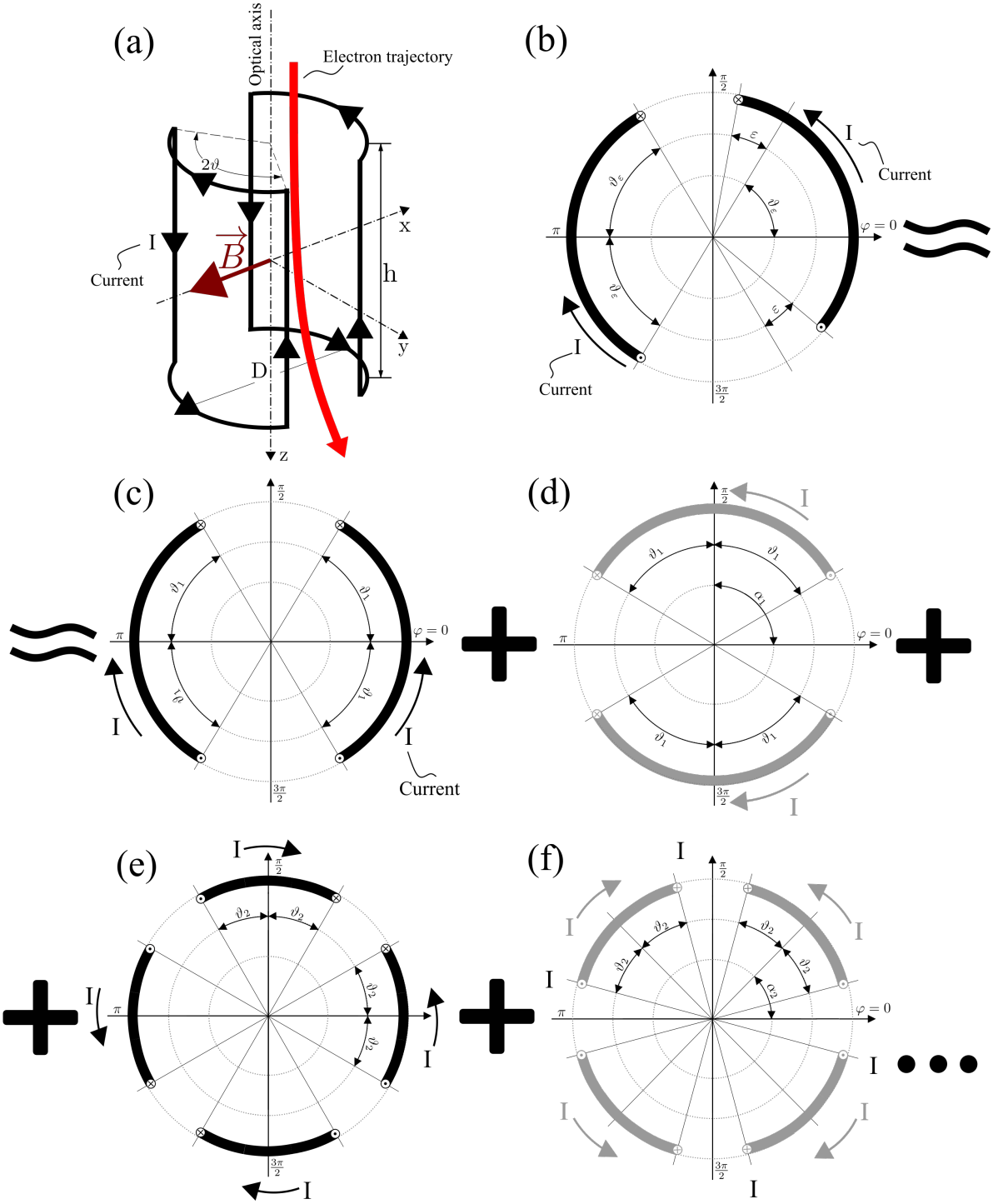

Fig. 3.2: (a): The geometry of the saddle deflection coil. (b): An axial view of the saddle deflection coil with the angle of misalignment ε. The direction of the current flow I. (c) - (f): Perfectly aligned multipoles of order m to generate reduced axial magnetic potentials $\psi_{m,p}$, which are used to approximate the multipole fields of misaligned dipole in (b).

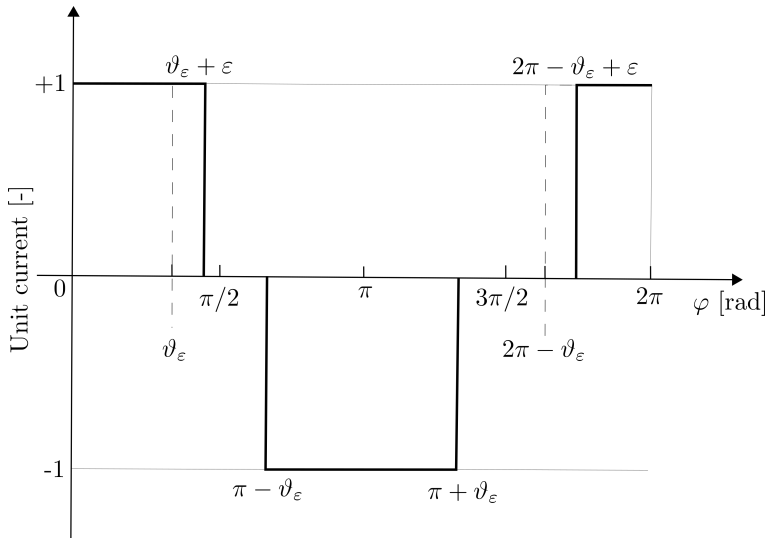

Fig. 3.3: A plot of the function $f_\varepsilon(\varphi)$ from eq. (3.14). A visualization of the unit current distribution for the misaligned saddle coil.

Angular excitation $f_\varepsilon(\varphi)$ can be written in the form of Fourier series defined in the sine-cosine form, [25] p. 11, with a period P as

$$f_\varepsilon(\varphi) = \frac{A_0}{2} + \sum_{m=1}^{\infty} \Big[A_m \cos\Big(\frac{2\pi}{P} m\varphi\Big) + B_m \sin\Big(\frac{2\pi}{P} m\varphi\Big)\Big] \tag{3.15}$$

and its Fourier coefficients are given by

$$A_0 = \frac{2}{P} \int_{\varphi_0}^{\varphi_0+P} f_\varepsilon(\varphi)\, d\varphi, \tag{3.16}$$

$$A_m = \frac{2}{P} \int_{\varphi_0}^{\varphi_0+P} f_\varepsilon(\varphi) \cos\Big(\frac{2\pi}{P} m\varphi\Big)\, d\varphi, \tag{3.17}$$

$$B_m = \frac{2}{P} \int_{\varphi_0}^{\varphi_0+P} f_\varepsilon(\varphi) \sin\Big(\frac{2\pi}{P} m\varphi\Big)\, d\varphi. \tag{3.18}$$

Let us consider the angular distribution of the excitation $f_\varepsilon(\varphi)$ with the period $P = 2\pi$ rad, the half-angle $\vartheta_\varepsilon = \pi/3$ rad and the angle of misalignment of the saddle coil ε in Fig. 3.2 (b). Then Fourier series coefficient A_0 is

$$A_0 = \frac{1}{\pi} \int_0^{2\pi} f_\varepsilon(\varphi)\, d\varphi = 0, \tag{3.19}$$

because multipole does not hold a focusing property, A_0 is always zero for multipole.

The Fourier series coefficient A_m is

$$A_m = \frac{1}{\pi}\Big[\int_{-\frac{\pi}{3}+\varepsilon}^{\frac{\pi}{3}+\varepsilon} +1 \cdot \cos\Big(m\varphi\Big) d\varphi + \int_{\frac{2\pi}{3}}^{\frac{4\pi}{3}} -1 \cdot \cos\Big(m\varphi\Big) d\varphi \Big], \tag{3.20}$$

$$A_m = \frac{2}{m\pi} \sin\frac{m\pi}{3} \Big[\cos(m\varepsilon) - \cos(m\pi) \Big]. \tag{3.21}$$

Similarly, the B_m is calculated

$$B_m = \frac{1}{\pi}\left[\int_{-\frac{\pi}{3}+\varepsilon}^{\frac{\pi}{3}+\varepsilon} +1 \cdot \sin(m\varphi)d\varphi + \int_{\frac{2\pi}{3}}^{\frac{4\pi}{3}} -1 \cdot \sin(m\varphi)d\varphi\right], \tag{3.22}$$

$$B_m = \frac{2}{m\pi}\sin\frac{m\pi}{3}\sin(m\varepsilon). \tag{3.23}$$

The calculation of the Fourier series coefficients A_m and B_m is greatly inspired by the infinite dipole method in section 3.1. Results for Fourier series coefficients A_m, B_m are in Fig. 3.4.

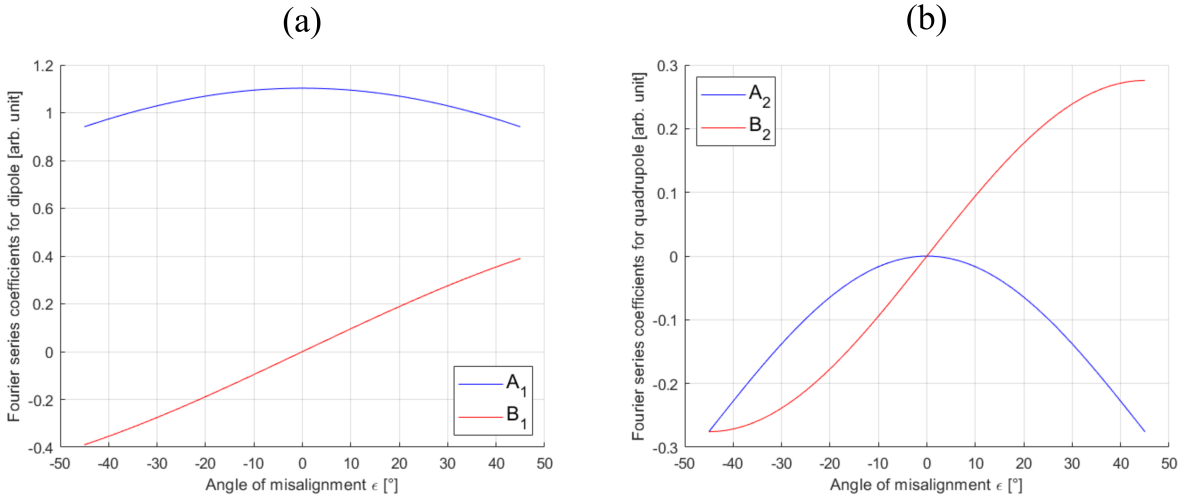

Fig. 3.4: (a): Fourier series coefficients for calculating dipole fields of the misaligned saddle coil. (b): Fourier series coefficients for calculating quadrupole fields of the misaligned saddle coil. It is calculated for the half-angle $\vartheta_\varepsilon = \pi/3$ rad and the misalignment angle ε.

The multipole components of the reduced axial magnetic potential of the misaligned saddle coil are calculated as

$$\psi_{m,\cos}(z) = \frac{A_m \psi_{m,p}(z)}{A_1(\varepsilon = 0)} \tag{3.24}$$

and

$$\psi_{m,\sin}(z) = \frac{B_m \psi_{m,p}(z)}{A_1(\varepsilon = 0)}, \tag{3.25}$$

where $\psi_{m,p}(z)$ is the reduced axial magnetic potential of the perfectly aligned multipole of order m with the half-angle $\vartheta_m = \pi/(3m)$ rad and with an equal amount of ampere-turns as for the misaligned dipole. Diameter D and height h of the added multipoles stay the same as well as it is for the original misaligned saddle coil. The reduced axial magnetic potential $\psi_{m,p}(z)$ for a perfectly aligned multipole of order m and with the corresponding half-angle ϑ_m can be calculated with EOD software.

The angle of rotation α_m between $\psi_{m,\cos}(z)$ and $\psi_{m,\sin}(z)$ is $\alpha_m = \pi/(2m)$ rad, see Fig 3.2. Therefore, no rotation of the fields $\psi_{m,\cos}$ is needed. The field $\psi_{m,\sin}$ has to be rotated by angle α_m in EOD software. Eq. (3.26) and eq. (3.27) produce no magnetic hexapole for $m = 3$, i.e., no three-fold astigmatism is produced because no such effect is observed for the half-angle $\vartheta = \pi/3$ rad of the saddle coil and even with the nonzero misalignment angle ε.

Instead of multiplying the reduced axial potentials $\psi_{m,p}(z)$ by normalized Fourier series coefficients, it is possible to apply it on the current I of the perfectly aligned multipoles, see Fig. 3.2: (c) - (f), as

$$I_{m,\cos} = \frac{A_m I}{A_1(\varepsilon = 0)} \tag{3.26}$$

and

$$I_{m,\sin} = \frac{B_m I}{A_1(\varepsilon = 0)}. \tag{3.27}$$

Currents $I_{m,\cos}$ and $I_{m,\sin}$ are used for to calculate the multipole components of the reduced axial magnetic potential of the misaligned saddle coil.

3.3. The corrected multipole method

New corrected multipole method is introduced for the multipole expansion of the angular distribution of the excitation of the saddle coil with broken symmetry for simplification of calculation of the magnetic field in the program for the design of electron microscopes EOD [21]. The corrected multipole method replaces the asymmetric angular distribution of the excitation of the saddle coil with infinitely many multipoles with a perfectly symmetric angular distribution of the excitation as in Fig. 3.5. The number of ampere-turns of the symmetrical multipoles is the same as for the asymmetric saddle coil. Diameter D and height h, see Fig. 3.2 (a), of the added multipoles stay the same as well as it is for the original misaligned saddle coil. Thus, the original magnetic field of the asymmetric saddle coil is replaced with the sum of magnetic fields of infinitely many symmetrical multipoles. No hexapole field is created by perfect dipole for the the half-angle $\vartheta_\varepsilon = \pi/3$ rad and as well as for the misaligned dipole. And higher multipoles are usually irrelevant.

The Fourier series approach is often helpful because it can be truncated, i.e., only the first few terms need to be used to approximate the original function. Moreover, it is also essential in our case that only the first few multipoles (dipoles, quadrupoles) have to be used for a good approximation of the original asymmetrical dipole.

Let us define an angular distribution of the excitation of the perfectly aligned saddle coil for dipole ($m = 1$) with half-angle ϑ_1, see Fig. 3.6, as

$$f_1(\varphi) = \begin{cases} 1 & \varphi \in [0, \vartheta_1)\,, \\ 0 & \varphi \in [\vartheta_1, \pi - \vartheta_1)\,, \\ -1 & \varphi \in [\pi - \vartheta_1, \pi + \vartheta_1)\,, \\ 0 & \varphi \in [\pi + \vartheta_1, 2\pi - \vartheta_1)\,, \\ 1 & \varphi \in [2\pi - \vartheta_1, 2\pi]\,. \end{cases} \tag{3.28}$$

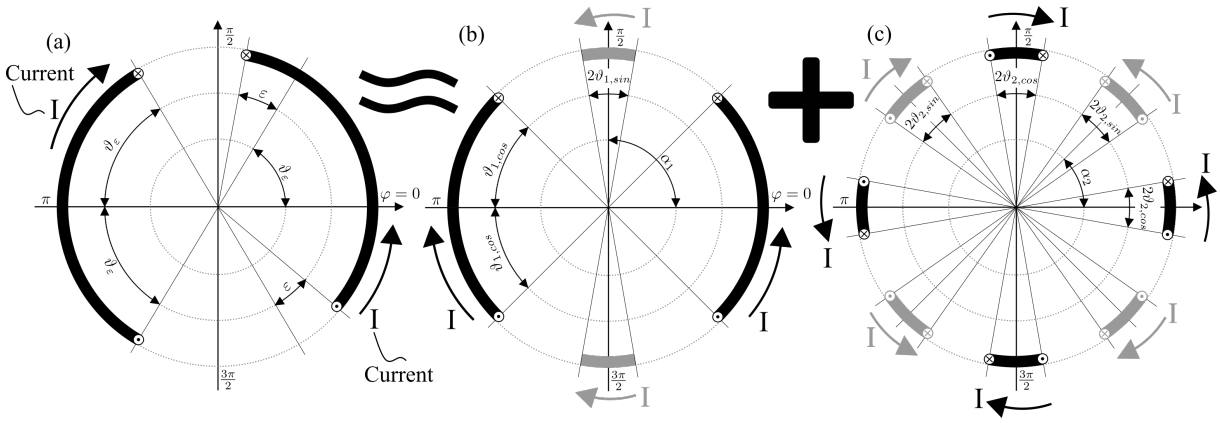

Fig. 3.5: (a): The angular distribution of the excitation for the asymmetrical saddle coil with half-angle ϑ_ε and angle of misalignment ε from eq. (3.6). This asymmetrical saddle coil is approximated by perfectly symmetric angular distributions of two dipoles in (b). The cosine part f_1 of the angular distribution is marked with black stripes and the sine part f_1 with gray stripes. The angle between the sine and cosine dipole parts is $\alpha_1 = \pi/2$ rad. In (c), there is the symmetric angular distribution of two quadrupoles from eq. (3.7). The sine part f_2 of the angular distribution is marked with black stripes, and the sine part f_2 with gray stripes. The angle between the sine and cosine dipole quadrupole parts is $\alpha_2 = \pi/4$ rad. The goal is to find the half-angles $\vartheta_{m,\cos}$ and $\vartheta_{m,\sin}$.

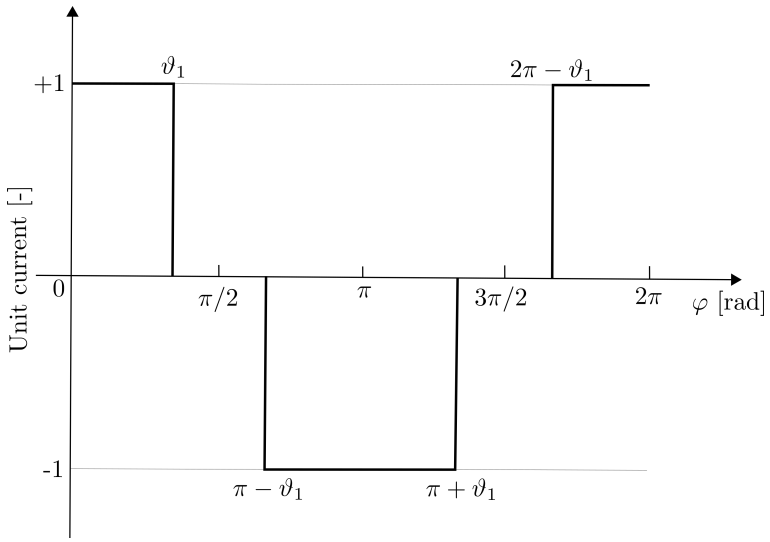

Fig. 3.6: A plot of the function $f_1(\varphi)$ from eq. (3.28). A visualization of the unit current distribution for the perfectly aligned saddle deflection coil with the half-angle ϑ_1.

Angular distribution of the excitation of the perfectly aligned quadrupole ($m = 2$) with a half-angle ϑ_2 , see Fig. 3.7, is defined as

$$f_2(\varphi) = \begin{cases} 1 & \varphi \in [0, \vartheta_2)\,, \\ 0 & \varphi \in [\vartheta_2, \pi/2 - \vartheta_2)\,, \\ -1 & \varphi \in [\pi/2 - \vartheta_2, \pi/2 + \vartheta_2)\,, \\ 0 & \varphi \in [\pi/2 + \vartheta_2, \pi - \vartheta_2)\,, \\ 1 & \varphi \in [\pi - \vartheta_2, \pi + \vartheta_2)\,, \\ 0 & \varphi \in [\pi/2 + \vartheta_2, 3\pi/2 - \vartheta_2)\,, \\ -1 & \varphi \in [3\pi/2 - \vartheta_2, 3\pi/2 + \vartheta_2)\,, \\ 0 & \varphi \in [3\pi/2 + \vartheta_2, 2\pi - \vartheta_2)\,, \\ 1 & \varphi \in [2\pi - \vartheta_2, 2\pi]\,. \end{cases} \tag{3.29}$$

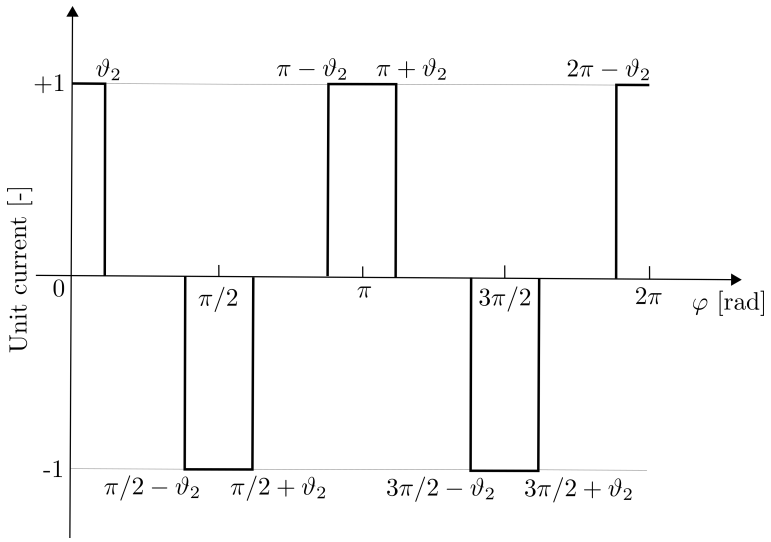

Fig. 3.7: A plot of the function $f_2(\varphi)$ from (3.29). A visualization of the unit current distribution of the perfectly aligned quadrupole ($m = 2$) with the half-angle ϑ_2.

Similarly, the hexapole and octupole angular distribution of the excitation could be defined. The general function $f_m(\varphi)$ of unit current distribution for multipole of order m with the half-angle ϑ_m is

$$f_m(\varphi) = \sum_{k=0}^{2m} (-1)^k \chi_{[\frac{k\pi}{m} - \vartheta_m; \frac{k\pi}{m} + \vartheta_m]}, \tag{3.30}$$

where $\chi_I : X \to \{0, 1\}$ is the indicator function of a subset I of a set X defined as

$$\chi_I(\varphi) := \begin{cases} 1 & \text{if } \varphi \in I, \\ 0 & \text{if } \varphi \notin I. \end{cases} \tag{3.31}$$

The general multipole $f_m(\varphi)$ can be also defined as

$$f_m = \sum_{k=0}^{2m} (-1)^k H\left(\varphi - \left(\frac{k\pi}{m} - \theta_m\right)\right) H\left(\frac{k\pi}{m} + \theta_m - \varphi\right), \tag{3.32}$$

where $H(\varphi)$ is the Heaviside step function defined as

$$H(\varphi) := \begin{cases} 1, & \varphi > 0 \\ 0, & \varphi \leq 0 \end{cases}. \tag{3.33}$$

Now, the goal is to approximate the original angular distribution of the excitation of the misaligned saddle coil with the half-angle $\vartheta_\varepsilon = \pi/3$ rad and the angle of misalignment ε by perfectly aligned multipoles with angular distributions of the excitation with the half angles ϑ_m as in Fig. 3.5. Therefore, half-angles $\vartheta_{m,\cos}$ and $\vartheta_{m,\sin}$ must be found.

3.3.1. Numerical solution

The half angles of multipoles $\vartheta_{m,\cos}$ and $\vartheta_{m,\sin}$ are calculated by equalization of Fourier series coefficients A_m and B_m, eq. (3.17) and (3.18), for $f_\varepsilon(\varphi)$ and for Fourier series coefficients a_m of the particular multipole such as $f_1(\varphi)$ and $f_2(\varphi)$ or generally $f_m(\varphi)$ as

$$A_m = a_m, \tag{3.34}$$

$$B_m = a_m. \tag{3.35}$$

Coefficient b_m could be used instead of a_m in eq. (3.35) as well, but only if the multipole $f_m(\varphi)$ is rotated.

The equations (3.34) and (3.35) can be rewritten

$$\int_0^{2\pi} f_\varepsilon(\varphi)\cos(m\varphi)\,d\varphi = \int_0^{2\pi} f_m(\varphi)\cos(m\varphi)\,d\varphi, \tag{3.36}$$

$$\int_0^{2\pi} f_\varepsilon(\varphi)\sin(m\varphi)\,d\varphi = \int_0^{2\pi} f_m(\varphi)\cos(m\varphi)\,d\varphi. \tag{3.37}$$

Equations (3.36) and (3.37) can be solved for $\vartheta_{m,\cos}$ and $\vartheta_{m,\sin}$ by use of numerical method such as the bisection method.

3.3.2. Analytical solution

The corrected multipole method can be also solved analytically to find the particular half-angle $\vartheta_{m,\cos}$ and $\vartheta_{m,\sin}$. Let us calculate the Fourier series coefficients of general symmetric multipole $f_m(\varphi)$, eq. (3.30), with a period $P = 2\pi$. The 0^{th} coefficient is

$$a_{m,0} = \frac{1}{\pi}\int_0^{2\pi} f_m(\varphi)d\varphi = \frac{1}{\pi}\int_0^{2\pi}\sum_{k=0}^{2m}(-1)^k\chi_{[\frac{k\pi}{m}-\vartheta_m;\frac{k\pi}{m}+\vartheta_m]}d\varphi = 0, \tag{3.38}$$

where m signifies the m^{th} order of multipole function $f_m(\varphi)$ and zero index signifies the 0^{th} coefficients of the Fourier series. $a_{m,l}$ signifies the m^{th} order of multipole function $f_m(\varphi)$ and l signifies the l^{th} coefficients of the Fourier series as

$$a_{m,l} = \frac{1}{\pi}\int_0^{2\pi} f_m(\varphi)\cos(l\varphi)d\varphi = \frac{1}{\pi}\int_0^{2\pi}\sum_{k=0}^{2m}(-1)^k\chi_{[\frac{k\pi}{m}-\vartheta_m;\frac{k\pi}{m}+\vartheta_m]}\cos(l\varphi)d\varphi \tag{3.39}$$

$$= \frac{1}{\pi}\sum_{k=0}^{2m}\int_0^{2\pi}(-1)^k \chi_{[\frac{k\pi}{m}-\vartheta_m;\frac{k\pi}{m}+\vartheta_m]}\cos(l\varphi)d\varphi \tag{3.40}$$

$$= \frac{1}{\pi}\sum_{k=0}^{2m}\int_{\max\{0,\frac{k\pi}{m}-\vartheta_m\}}^{\min\{2\pi,\frac{k\pi}{m}+\vartheta_m\}}(-1)^k\cos(l\varphi)d\varphi \tag{3.41}$$

$$= \frac{1}{\pi l}\Bigg\{\sin(l\vartheta_m) - \sin\big[l(2\pi-\vartheta_m)\big] + \sum_{k=0}^{2m-1}(-1)^k\bigg[\sin\Big(l\big(\frac{k\pi}{m}+\vartheta_m\big)\Big) - \sin\Big(l\big(\frac{k\pi}{m}-\vartheta_m\big)\Big)\bigg]\Bigg\} \tag{3.42}$$

$$= \frac{2}{\pi l}\Big[\sin(l\vartheta_m) + \sum_{k=0}^{2m-1}(-1)^k\cos\Big(\frac{k\pi l}{m}\Big)\sin(l\vartheta_m)\Big]. \tag{3.43}$$

$$a_{m,l} = \frac{2}{\pi l}\sum_{k=0}^{2m}(-1)^k\cos\Big(\frac{k\pi l}{m}\Big)\sin(l\vartheta_m). \tag{3.44}$$

Similarly for the sine part

$$b_{m,l} = \frac{1}{\pi}\int_0^{2\pi} f_m(\varphi)\sin(l\varphi)d\varphi = \frac{1}{\pi}\int_0^{2\pi}\sum_{k=0}^{2m}(-1)^k\chi_{[\frac{k\pi}{m}-\vartheta_m;\frac{k\pi}{m}+\vartheta_m]}\sin(l\varphi)d\varphi = 0. \tag{3.45}$$

$b_{m,l}$ is equal to zero, because $f_m(\varphi)$ is an even function.

To replace the original misaligned saddle coil winding with symmetrical multipoles to create the same magnetic field, corresponding Fourier series coefficients has to be equal. We are interested only in l^{th} coefficients of the Fourier series of the m^{th} order of multipole function $f_m(\varphi)$, so $m = l$. A_m is the Fourier series coefficient of $f_\varepsilon(\varphi)$, eq. (3.14). For $\vartheta_{m,\cos}$ from eq. (3.22) and eq. (3.44)

$$A_m = a_{m,l}, \tag{3.46}$$

for $m = l$

$$\frac{2}{m\pi}\sin\frac{m\pi}{3}\Big[\cos(m\varepsilon) - \cos(m\pi)\Big] = \frac{2}{m\pi}\sum_{k=0}^{2m}(-1)^k\cos\Big(\frac{k\pi m}{m}\Big)\sin(m\vartheta_{m,\cos}), \tag{3.47}$$

$$\vartheta_{m,\cos} = \frac{1}{m}\arcsin\left(\frac{\sin\frac{m\pi}{3}\big[\cos(m\varepsilon)-\cos(m\pi)\big]}{\sum_{k=0}^{2m}(-1)^k\cos(k\pi)}\right) \quad \text{for } -\frac{\pi}{2} \le \vartheta_{m,\cos} \le \frac{\pi}{2}. \tag{3.48}$$

For $\vartheta_{m,\sin}$ from eq. (3.23) and eq. (3.44)

$$B_m = a_{m,l}, \tag{3.49}$$

for $m = l$

$$\frac{2}{m\pi}\sin\frac{m\pi}{3}\sin(m\varepsilon) = \frac{2}{m\pi}\sum_{k=0}^{2m}(-1)^k\cos\Big(\frac{k\pi m}{m}\Big)\sin(m\vartheta_{m,\sin}), \tag{3.50}$$

$$\vartheta_{m,\sin} = \frac{1}{m}\arcsin\left(\frac{\sin\frac{m\pi}{3}\sin(m\varepsilon)}{\sum_{k=0}^{2m}(-1)^k\cos(k\pi)}\right) \quad \text{for } -\frac{\pi}{2} \le \vartheta_{m,\sin} \le \frac{\pi}{2}. \tag{3.51}$$

Equations (3.48) and (3.51) are valid for the half-angle $\vartheta_\varepsilon = \pi/3$ rad of the misaligned saddle coil. The solutions for half-angles ϑ_m can be seen in Fig. 3.8.

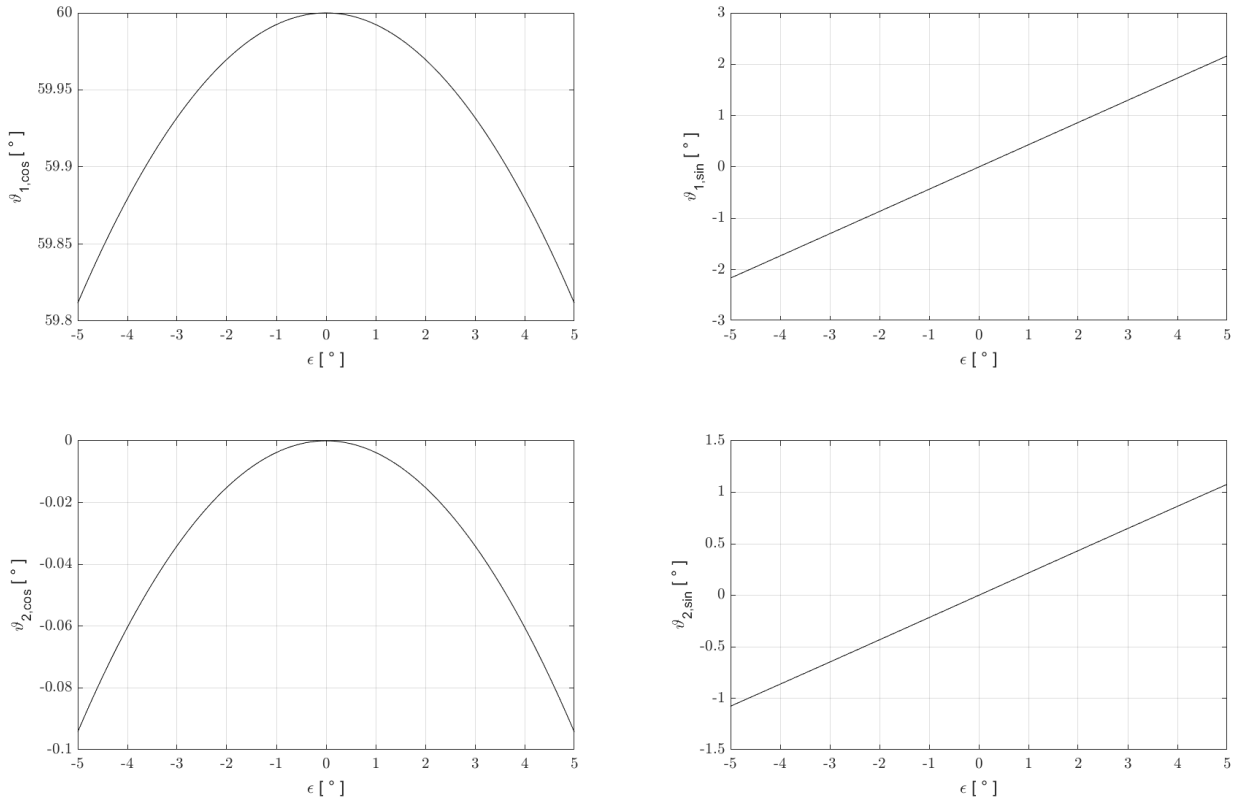

Fig. 3.8: Analytically calculated half-angles ϑ_m by the corrected multipole method for the misaligned saddle coil with half-angle $\vartheta_\varepsilon = \pi/3$ rad and the angle of misalignment ε from eq. (3.48) and (3.51).

Thus, the original multipole magnetic field of the misaligned dipole, which is generated by the angular distribution of the excitation of the saddle coil with broken symmetry f_ε, is approximated for $m = 1$ by two magnetic fields of dipoles rotated by $\pi/2$ rad against each other. Their magnetic field is generated by the angular distributions of the excitation of the saddle coils with half-angles $\vartheta_{1,\cos}$ and $\vartheta_{1,\sin}$. To approximate further, the magnetic field of quadrupoles $m = 2$ generated by f_ε quadrupoles with the angular distribution of the excitation with half-angles $\vartheta_{2,\cos}$ and $\vartheta_{2,\sin}$ need to be added. Quadrupoles are rotated by $\pi/4$ rad against each other. For $m = 3$ and $\vartheta_\varepsilon = \pi/3$ rad, half-angles are $\vartheta_{2,\cos} = 0$ rad and $\vartheta_{2,\sin} = 0$ rad. No hexapole fields are created by the misaligned dipole for the half-angle $\vartheta_\varepsilon = \pi/3$ rad. For even more precise approximation $m = 4$, octupoles with half-angles $\vartheta_{4,\cos}$, $\vartheta_{4,\sin}$ can be added. Multipoles of order m are always rotated by $\pi/(2m)$ rad against each other.

Then, the half-angles of multipoles $\vartheta_{1,\cos}$, $\vartheta_{1,\sin}$, $\vartheta_{2,\cos}$, $\vartheta_{2,\sin}$ can be used to calculate magnetic multipoles in the EOD software to approximate the original magnetic multipole fields of the misaligned saddle coil. However, it is possible that replacing the original asymmetric windings with several and even infinitely many symmetrical windings will

produce its own parasitic multipoles magnetic fields. For example, if dipole's half-angle is not $\vartheta_{1,\cos} = \pi/3$ rad, additional hexapole and decapole is generated. If quadrupole's half-angle is not $\vartheta_{2,\cos} = \pi/6$ rad, additional dodecapole is generated. However, they are negligible compared to the magnetic dipoles and quadrupoles produced by the asymmetric winding, which are of primary interest in the first place.

3.4. 2D and 3D finite element method

The 3D finite element method simulations were carried out to quantitatively as well as qualitatively confirm multipole fields of misaligned saddle coil for methods mentioned in the Section 3.2 and 3.3. The 3D solution of the field was computed in the software COMSOL Multiphysics version 5.4 with AC/DC module. There are some disadvantages of 3D simulation compared to 2D simulation. Rather, sizeable random-access memory is needed, and the computational time is usually substantially longer. Therefore, the mesh is not as dense as the 2D simulation, and the relative accuracy is lower. Few aspects of 2D and 3D simulation are summed up in Table 3.1. A model of the saddle deflection with the iron core in Fig. 3.9. The magnetic induction $\vec{B}$ of the misaligned saddle coil was exported from COMSOL to EOD software. The magnetic induction $\vec{B}$ was accurately interpolated by use of REAF [24]. The interpolation method interpolates all multipole components up to order $m = 8$ as well as calculates corresponding reduced axial magnetic potentials. The dimensions of the misaligned saddle coil can be found in Fig. 2.7.

Table 3.1: A comparison of 2D and 3D simulations.

	2D FEM computation	3D FEM computation
Software	EOD	COMSOL
Finite element method	First order	Second order
Computational time	~8 s	~10 min
Relative accuracy	up to 10^{-16}	10^{-9}
Number of mesh elements	~0.4 milion	~3 milion
Minimum used element size	0.02 mm	0.33 mm
RAM requirements	~50 MB	~30 GB

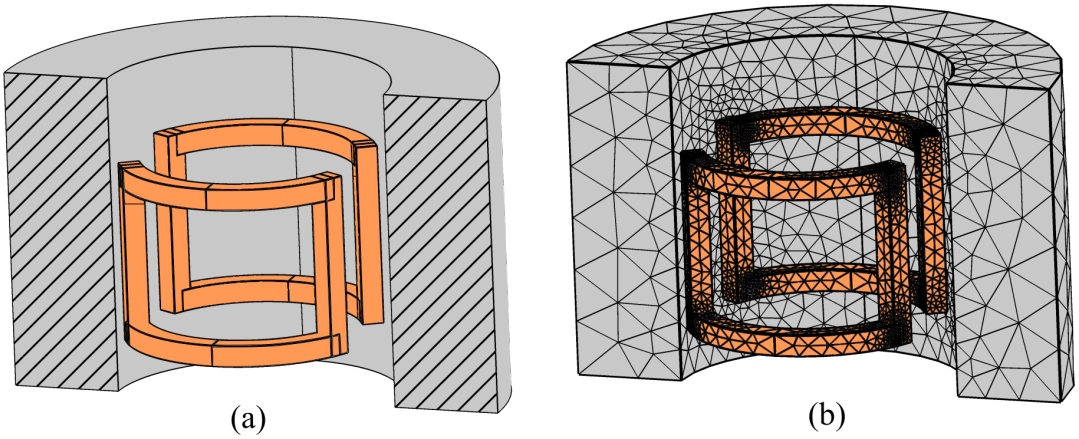

Fig. 3.9: (a): A representation of the saddle deflection coil with a cross section of the iron core in the COMSOL Multiphysics software. Dimensions corresponds to Fig. 2.7. (b): A visualization of the mesh elements.

The CAD design of the saddle coil and with the core from the EOD software is in Fig. 3.10.

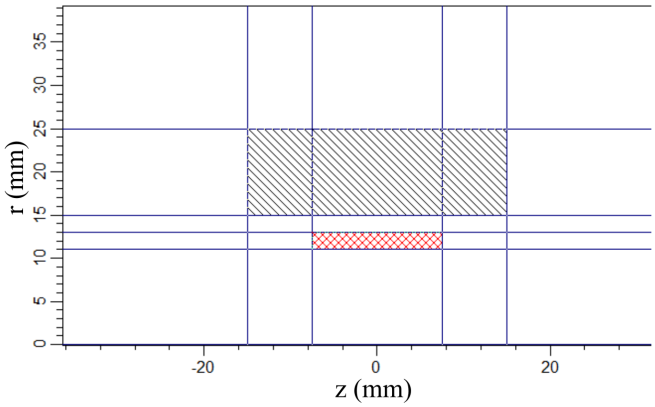

Fig. 3.10: CAD design of the saddle deflection coil from EOD software from Fig. 2.7. Saddle coil in red, iron core in black.

The material of the core is set to be a general iron. For linear computation (no saturation effect of magnetic material) is relative permeability $\mu_r = 2500$. For nonlinear computation (with saturation of magnetic material) is the magnetization curve in Fig. 3.11.

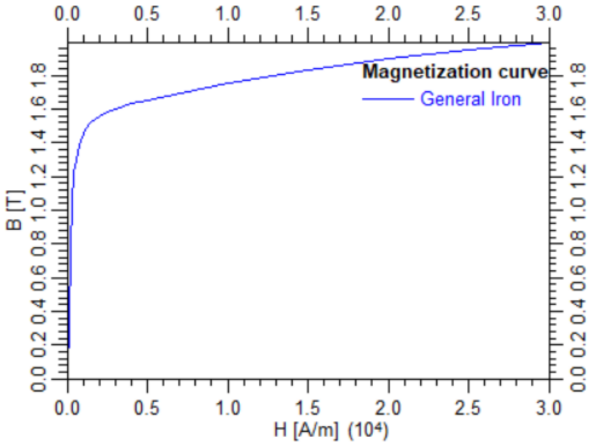

Fig. 3.11: The magnetization curve of general iron used for calculation in EOD software.

Dirichlet boundary condition was used for calculation of multipoles in EOD. Magnetic insulator, $\vec{n} \times \vec{A} = 0$, is the boundary condition for COMSOL simulations. $\vec{n}$ is the normal vector to the boundary and $\vec{A}$ is magnetic vector potential.

No significant difference between materials such as general iron and permendur was found for the standard deflection system with a core for 10 At. The relative difference for the maximum of the reduced axial magnetic potential was found to be less than 0.05 %. No significant difference was found for the core lengths either. The relative difference between the core length $6h$ and $2h$ for the maximum of the reduced axial magnetic potential was found to be less than 0.02 %. So, the length of the saddle coil core was chosen to be $2h$. No significant saturation effect of the coil core material was found for the ampere-turn 10 At. The relative difference between the linear computation (no saturation of magnetic materials) and the non-linear computation (with a saturation of the magnetic material) in the maximum of the reduced axial magnetic potential was found to be less than 0.01 %.

4. Results of simulations

This chapter deals with comparing multipole reduced axial magnetic potentials of the misaligned saddle deflection with decency on the angle of misalignment ε. It shows the results of implementing the normalized Fourier series coefficients method and the corrected multipole method to 2D FEM solutions of EOD software. The 3D FEM solutions are shown as well. All simulations were carried out for the EOD saddle coil design in Fig. 3.10 and its closest representation in Comsol Multiphysics software in Fig. 2.7. The half-angle of the saddle coil is set to be $\vartheta_\varepsilon = \pi/3$ rad and 10 At.

4.1. The perfect saddle coil

First, it is essential to compare the results of 2D and 3D FEM for the perfect $\varepsilon = 0$ rad saddle coil, see Fig. 4.1. Although the reduced dipole axial magnetic potential $\psi_{1,\cos}$ does not equal for all points on the Z axis, the difference is considered negligible. It is interesting to point out that the percentage difference is under 10 % for Z axis from -15 mm to +15 mm. That corresponds to the length of the iron core. These results are an important benchmark for comparing multipole fields caused by the misalignment.

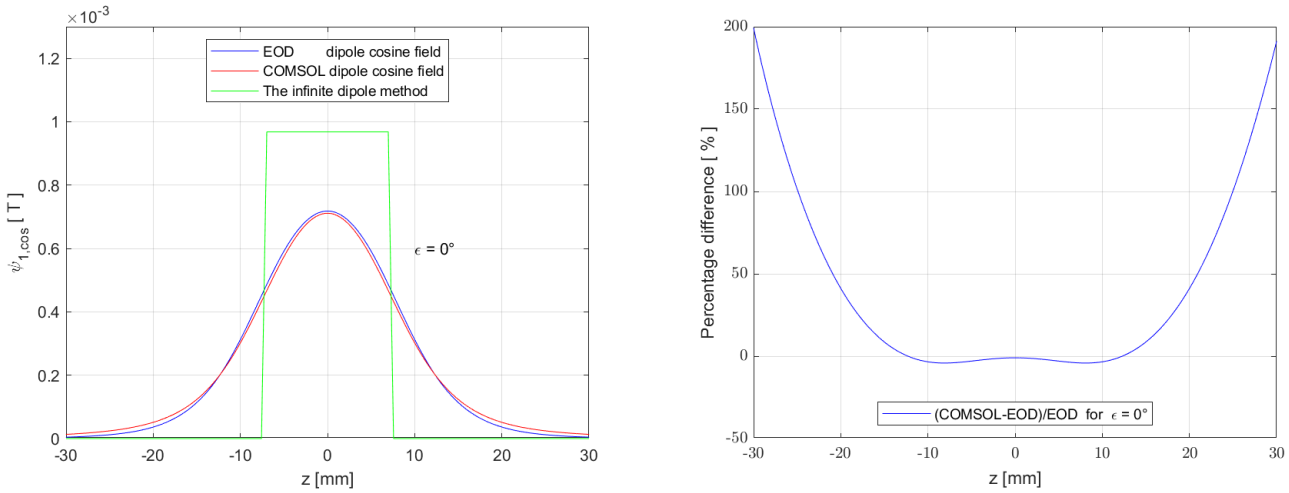

Fig. 4.1: On the left: The reduced dipole axial magnetic potential $\psi_{1,\cos}(z)$ for the 2D FEM EOD, the 3D FEM Comsol Multiphysics, and the infinite dipole method for the perfect saddle deflection coil. On the right: The percentage difference between the two.

4.2. Misaligned saddle coil

The values for the misalignment angle are set to be in the range of $\varepsilon = \pm 5°$. This range is sufficient to compare the behavior of multipole fields from the manufacturing point of view because standard manufacturing precision is usually $\varepsilon = \pm 2°$. The question of how to quantitatively compare multipole fields for each method now arises. Three approaches were chosen: plotting reduced multipole axial magnetic potentials for each method for $\varepsilon = 2°$, comparing values of global extrema of reduced multipole axial magnetic potentials, and

comparing the total area under the curve of reduced multipole axial magnetic potential for each method for varying angle of misalignment ε.

4.2.1. Dipole cosine field

The reduced dipole axial magnetic potential $\psi_{1,\cos}$ varies only slightly for change in the misalignment angle ε, see Fig 4.2. The normalized Fourier series coefficients method and the corrected multipole method show the same results. The 3D FEM Comsol method exhibit excellent correspondence with 2D models, and it argues in favor of the validity of 2D models for $\psi_{1,\cos}$. The percentage difference between the 2D and the 3D FEM is under 1 % for global extrema and under 3 % for the area under the curve, see Fig 4.3.

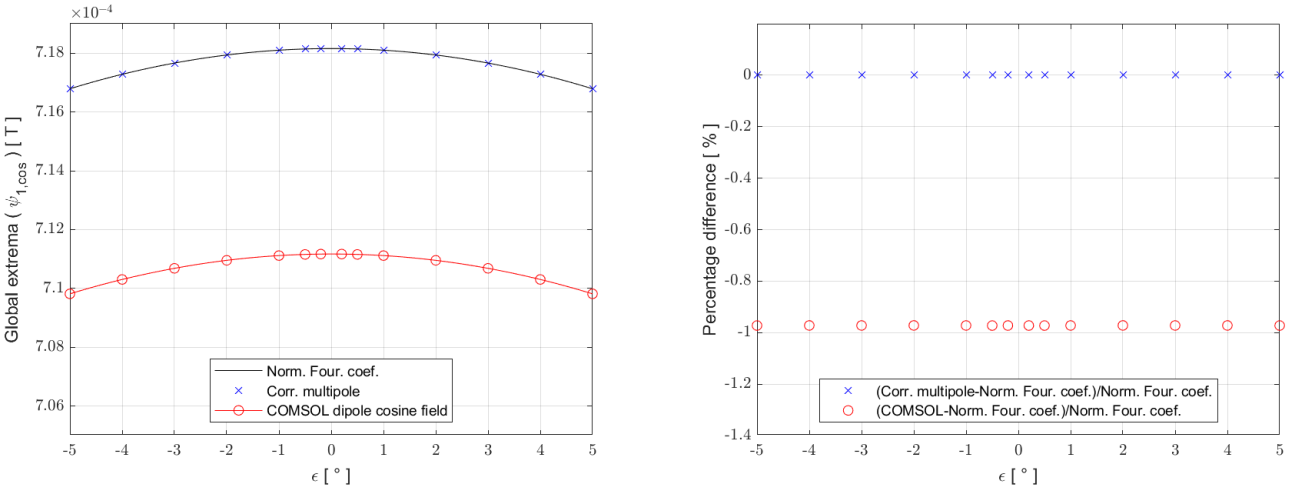

Fig. 4.2: On the left: Global extrema of reduced dipole axial magnetic potential $\psi_{1,\cos}(\varepsilon)$ for the normalized Fourier series coefficients method, the corrected multipole method, and 3D FEM Comsol Multiphysics with dependence on the angle of misalignment ε. On the right: The percentage difference between the methods.

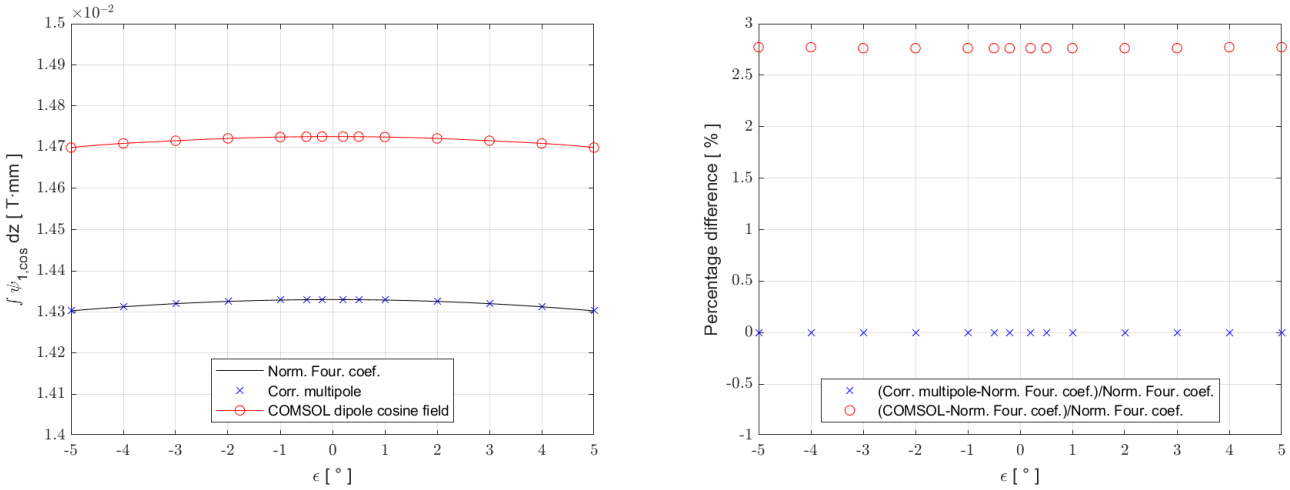

Fig. 4.3: On the left: The integral value of reduced dipole axial magnetic potential $\psi_{1,\cos}(\varepsilon)$ for the normalized Fourier series coefficients method, the corrected multipole method, and the 3D FEM Comsol Multiphysics with a dependence on the angle of misalignment ε. On the right: The percentage difference between the methods.

4.2.2. Dipole sine field

If the angle of misalignment ε is non-zero, the deflection dipole sine field $\psi_{1,\sin}$ arises to the existence, and it is perpendicular to the original dipole cosine field $\psi_{1,\cos}$, see Fig 4.4. Reduced dipole axial magnetic potential $\psi_{1,\sin}$ expresses an effect that the magnitude of the field is linearly dependent on the angle of misalignment ε for $\sin\varepsilon \approx \varepsilon$. However, it is approximately three orders of magnitude lower compared to the main deflection field $\psi_{1,\cos}$ for $\varepsilon = \pm 2°$. The 3D FEM Comsol method appears to be saying that although 2D models vary slightly, results ultimately claim the validity of 2D models for $\psi_{1,\sin}$. The percentage difference between the 2D and 3D FEM is under 1 % for global extrema, see Fig 4.6, and under 3 % for the area under the curve, see Fig 4.7. The normalized Fourier series coefficients method and the corrected multipole method present the same results, see Fig 4.5.

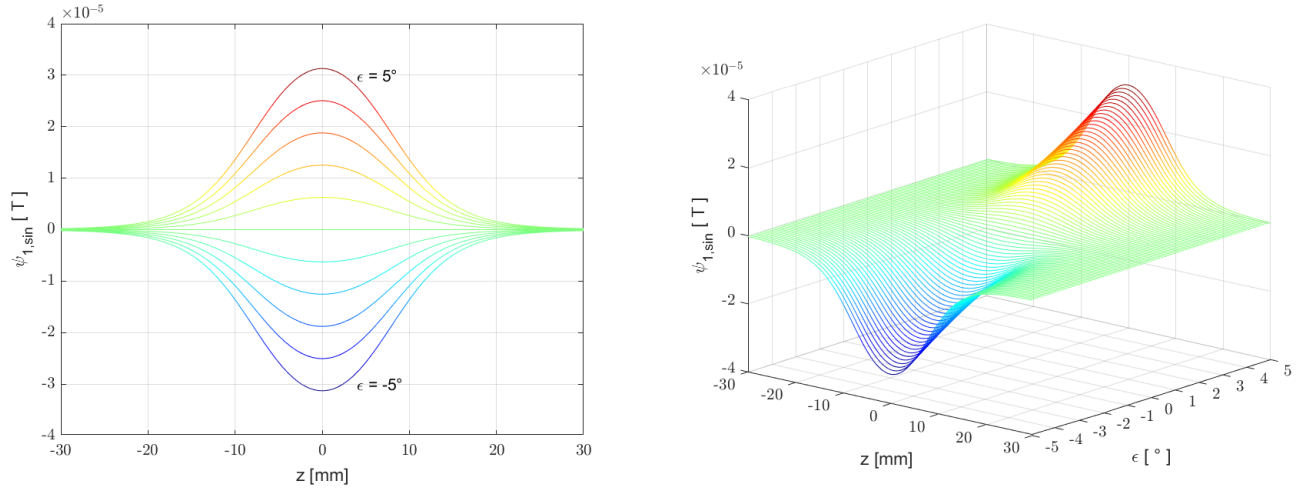

Fig. 4.4: On the left: Reduced dipole axial magnetic potential $\psi_{1,\sin}(z)$ for the normalized Fourier series coefficients method with a dependence on the angle of misalignment $\varepsilon \in \{5°, 4°, 3°, 2°, 1°, 0°, -1°, -2°, -3°, -4°, -5°\}$. On the right: Visualization of $\psi_{1,\sin}(z, \varepsilon)$.

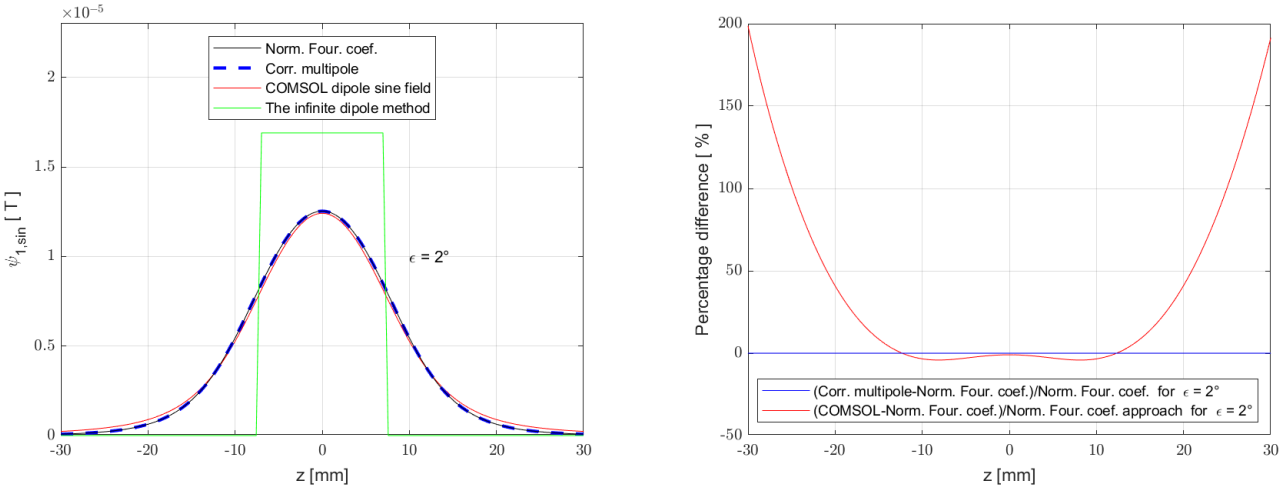

Fig. 4.5: On the left: The reduced dipole axial magnetic potential $\psi_{1,\sin}(z)$ for the normalized Fourier series coefficients method, the corrected multipole method, the 3D FEM Comsol Multiphysics, and the infinite dipole method for the angle of misalignment $\varepsilon = 2°$. On the right: The percentage difference between the methods.

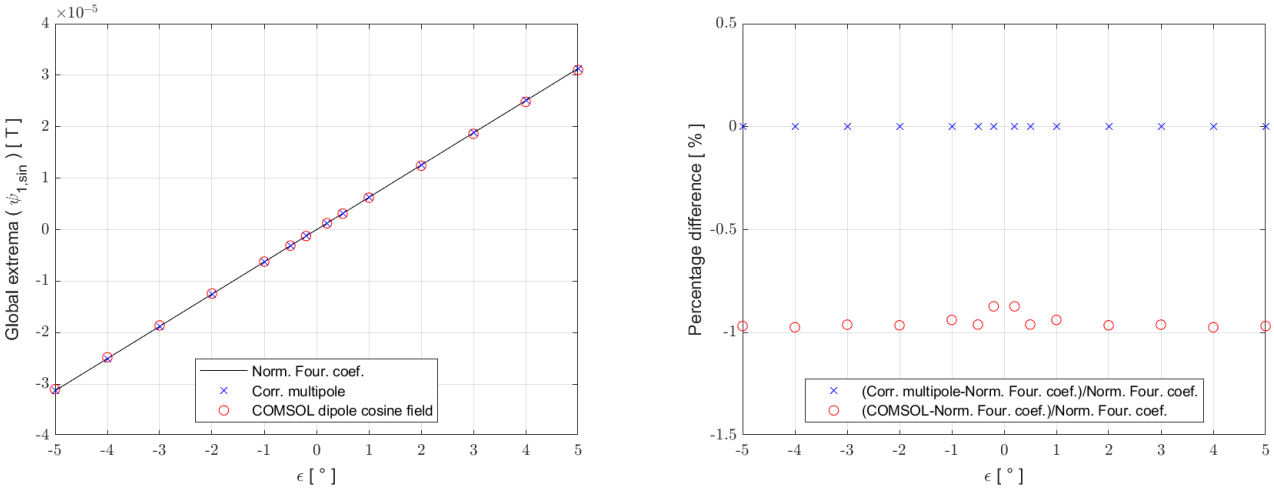

Fig. 4.6: On the left: Global extrema of the reduced dipole axial magnetic potential $\psi_{1,\sin}(z)$ for the normalized Fourier series coefficients method, the corrected multipole method, and the 3D FEM Comsol Multiphysics with a dependence on the angle of misalignment ε. On the right: The percentage difference between the methods.

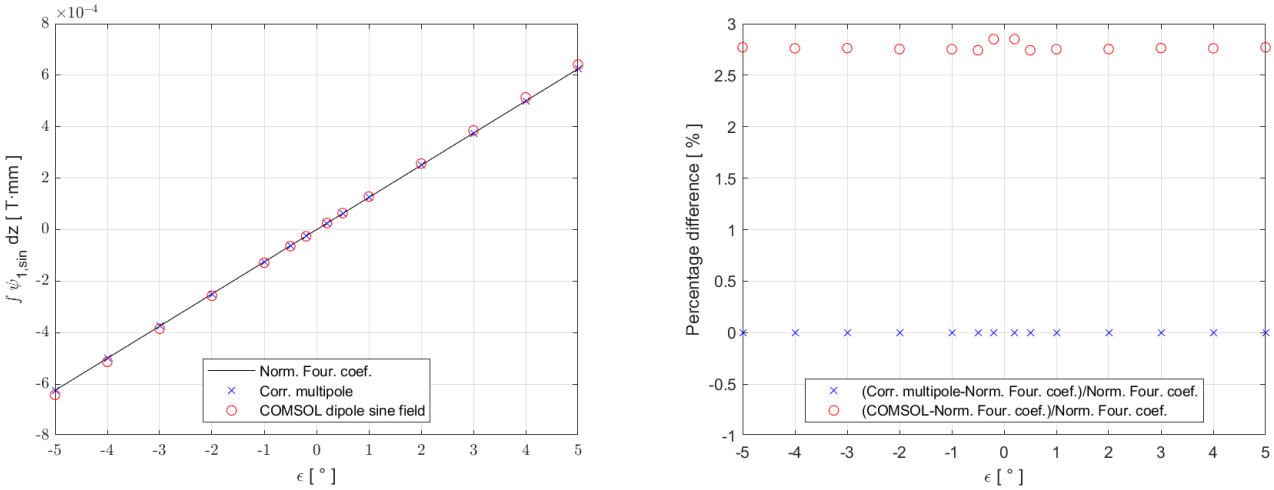

Fig. 4.7: On the left: Integral values of reduced dipole axial magnetic potential $\psi_{1,\sin}(z)$ for the normalized Fourier series coefficients method, the corrected multipole method, and the 3D FEM Comsol Multiphysics with dependence on the angle of misalignment ε. On the right: The percentage difference between the methods.

4.2.3. Quadrupole cosine field

The quadrupole cosine field shows that the reduced quadrupole axial magnetic potential $\psi_{2,\cos}$ comes into effect for the non-zero value of ε. It provides excellent examples of mechanical misalignment causing 2-fold astigmatism, see Fig 4.8. Underlying quadrupole cosine field's argument appears to be the fact that $\psi_{2,\cos}$ is negative, and it does increase approximately quadratically for $\varepsilon = \pm 5°$. The normalized Fourier series coefficients method and the corrected multipole method presents the same results, see Fig 4.9.

The cardinal issue for the 3D FEM Comsol method appears to be the relative accuracy of 10^{-9}. So, it is only one order of magnitude above the values of $\psi_{2,\cos}$, see Fig 4.9. However, the 3D FEM Comsol method approves the validity of the normalized Fourier series coefficients method and the corrected multipole method. The percentage difference between the 2D and 3D FEM is under 3 % for global extrema, see Fig 4.10, and under 5 % for area under the curve, see Fig 4.11. Both see an increase in the percentage difference around zero misalignment due to the relative accuracy of only 10^{-9} of the 3D FEM.

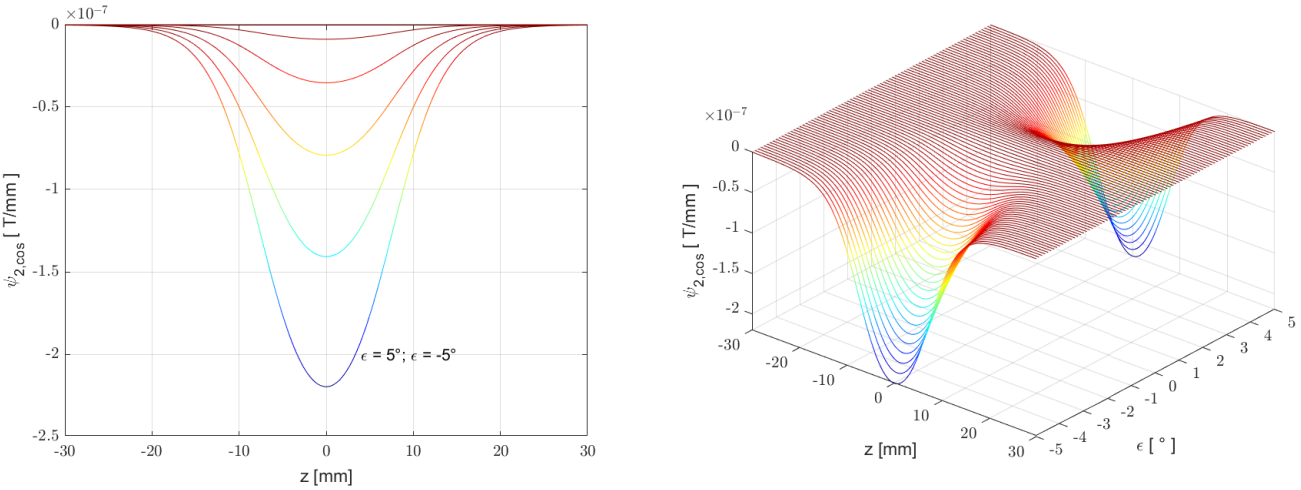

Fig. 4.8: On the left: The reduced quadrupole axial magnetic potential $\psi_{2,\cos}(z)$ for the normalized Fourier series coefficients method with a dependence on the angle of misalignment $\varepsilon \in \{5°, 4°, 3°, 2°, 1°, 0°, -1°, -2°, -3°, -4°, -5°\}$. On the right: Visualization of $\psi_{2,\cos}(z, \varepsilon)$.

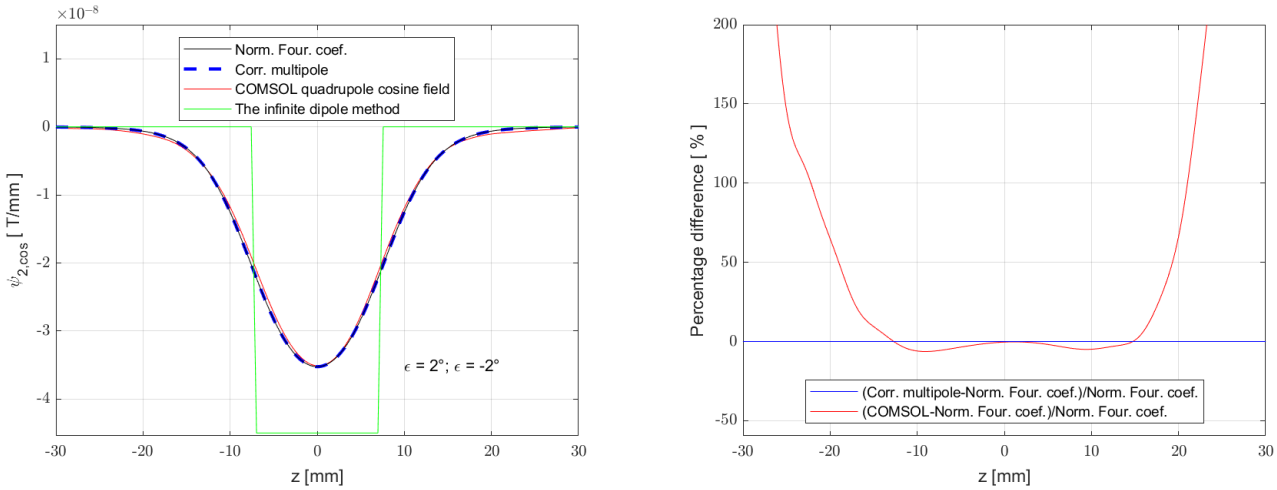

Fig. 4.9: On the left: Reduced quadrupole magnetic potential $\psi_{2,\cos}(z)$ for the normalized Fourier series coefficients method with a dependence on the angle of misalignment $\varepsilon = 2°$. On the right: Visualization of $\psi_{2,\cos}(z, \varepsilon)$.

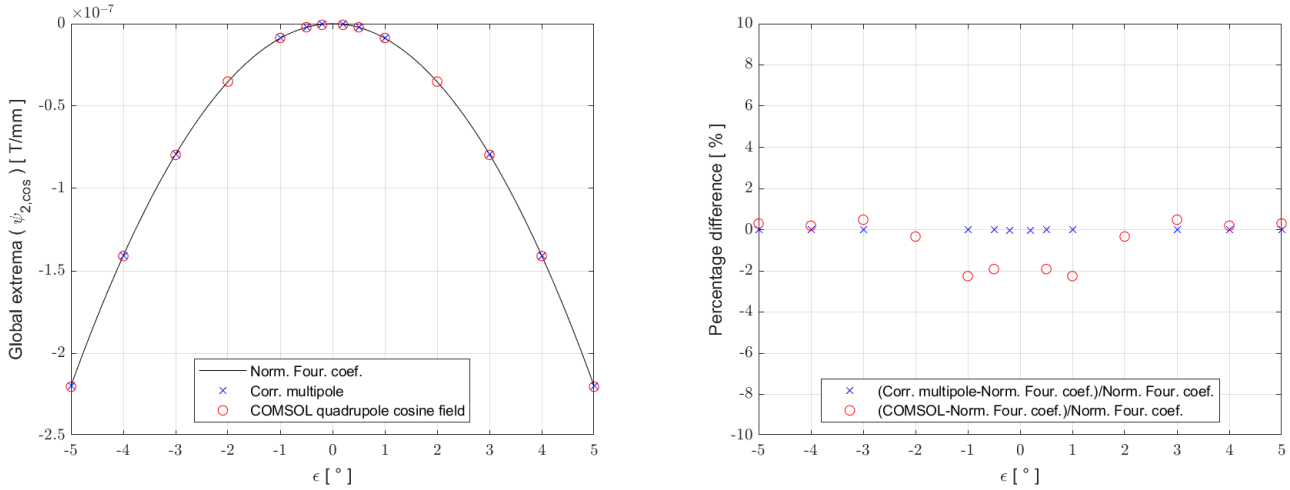

Fig. 4.10: On the left: Global extrema of reduced quadrupole axial magnetic potential $\psi_{2,\cos}(z)$ for the normalized Fourier series coefficients method, the corrected multipole method, and the 3D FEM Comsol Multiphysics with a dependence on the angle of misalignment ε. On the right: The percentage difference between the methods.

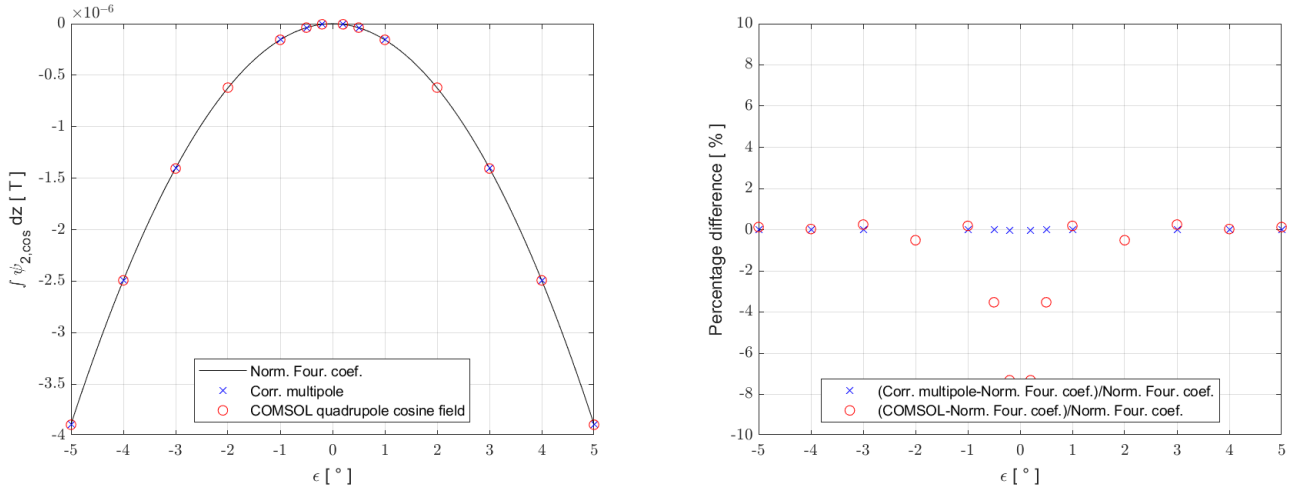

Fig. 4.11: On the left: Integral values of reduced quadrupole axial magnetic potential $\psi_{2,\cos}(z)$ for the normalized Fourier series coefficients method, the corrected multipole method, and the 3D FEM Comsol Multiphysics with a dependence on the angle of misalignment ε. On the right: The percentage difference between the methods.

4.2.4. Quadrupole sine field

The quadrupole sine field puts arguments forward that the reduced quadrupole axial magnetic potential $\psi_{2,\sin}$ is linearly increasing for $\sin\varepsilon \approx \varepsilon$ and is approximately one order of magnitude higher than $\psi_{2,\cos}$. Ultimately, the quadrupole sine field appears to be the predominant cause of the 2-fold astigmatism for $\varepsilon \pm 2°$. The normalized Fourier series coefficients method and the corrected multipole method present the same results, see Fig 4.12. The 3D FEM Comsol method approves the validity of the normalized Fourier

series coefficients method and the corrected multipole method. The percentage difference between the 2D and 3D FEM is under 0.5 % for global extrema, see Fig 4.14, and under 0.25 % for area under the curve, see Fig 4.15.

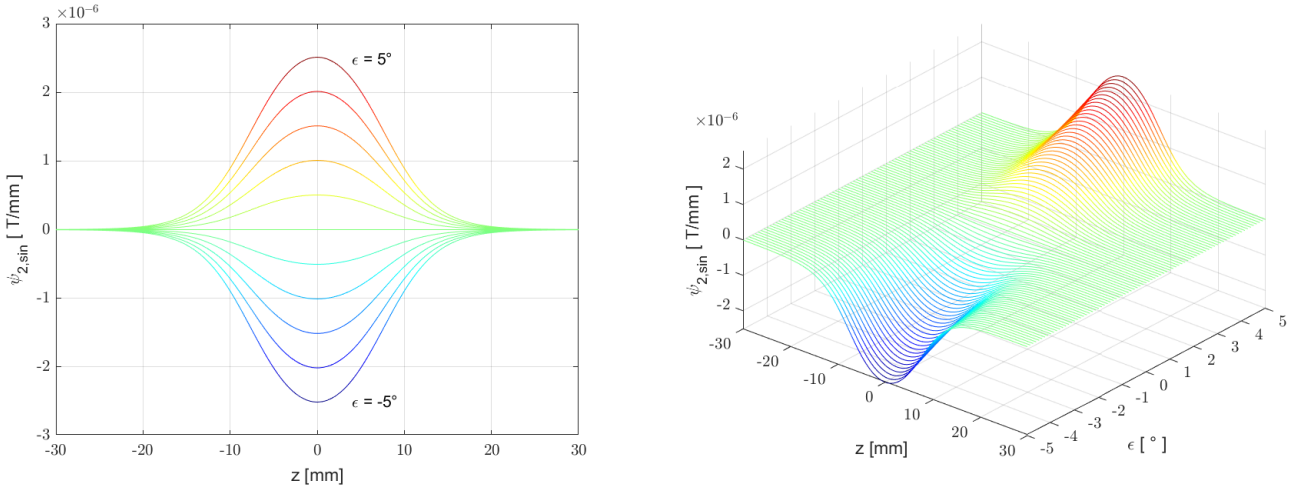

Fig. 4.12: On the left: The reduced quadrupole magnetic potential $\psi_{2,\sin}(z)$ for the normalized Fourier series coefficients method with dependence on the angle of misalignment $\varepsilon \in \{5°, 4°, 3°, 2°, 1°, 0°, -1°, -2°, -3°, -4°, -5°\}$. On the right: Visualization of $\psi_{2,\cos}(z, \varepsilon)$.

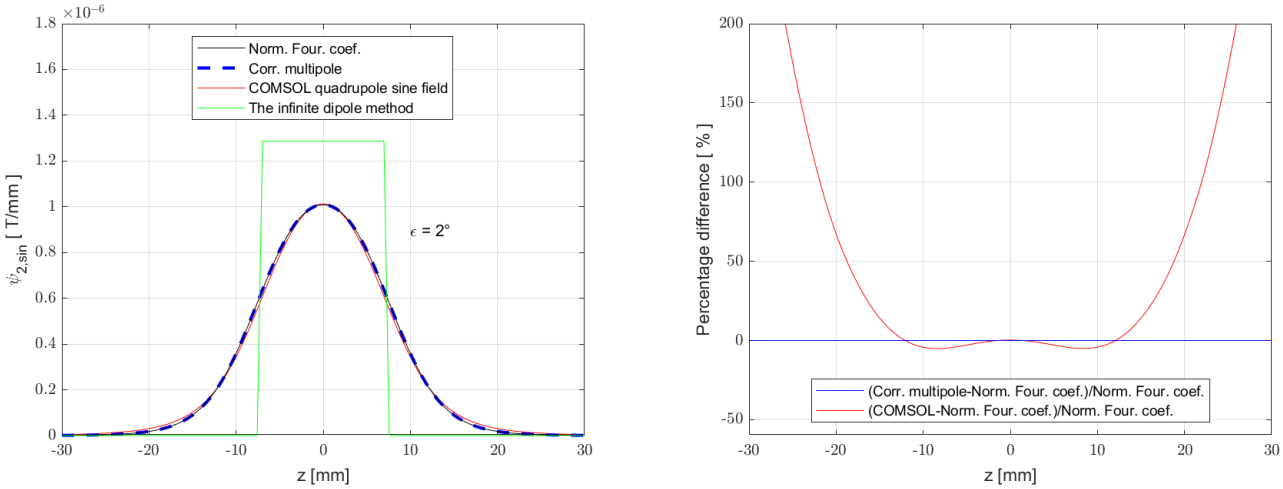

Fig. 4.13: On the left: Reduced quadrupole axial magnetic potential $\psi_{2,\sin}(z)$ for the normalized Fourier series coefficients method, the corrected multipole method, the 3D FEM Comsol Multiphysics, and the infinite dipole method for the angle of misalignment $\varepsilon = 2°$. On the right: Visualization of $\psi_{2,\sin}(z, \varepsilon)$.

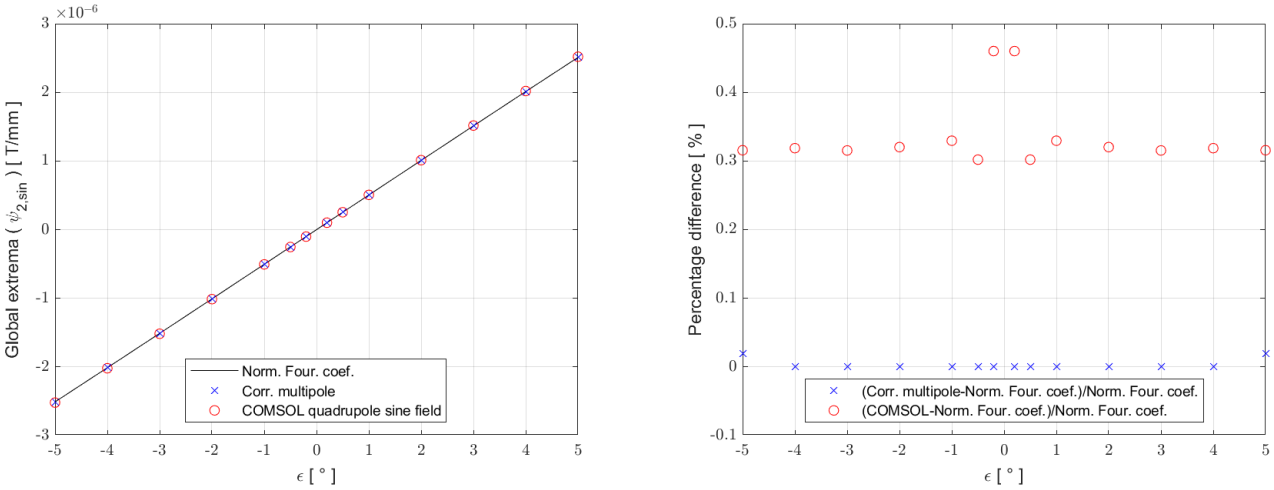

Fig. 4.14: On the left: Global extrema of reduced quadrupole axial magnetic potential $\psi_{2,\sin}(z)$ for the normalized Fourier series coefficients method, the corrected multipole method, and the 3D FEM Comsol Multiphysics with dependence on the angle of misalignment ε. On the right: The percentage difference between the methods.

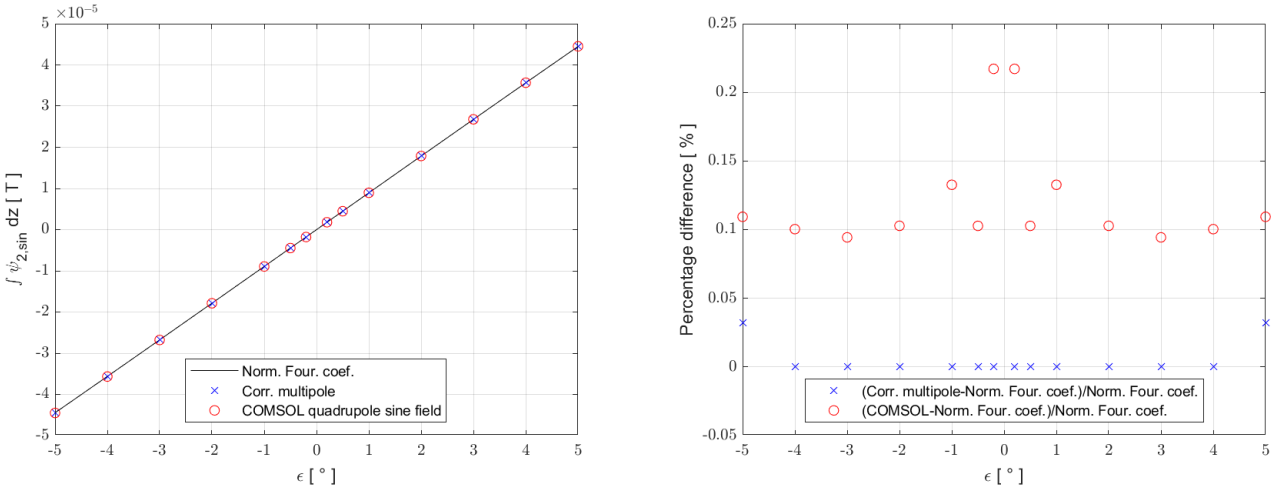

Fig. 4.15: On the left: Integral values of reduced quadrupole axial magnetic potential $\psi_{2,\cos}(z)$ for the normalized Fourier series coefficients method, the corrected multipole method, and the 3D FEM Comsol Multiphysics with dependence on the angle of misalignment ε. On the right: The percentage difference between the methods.

5. Experiment

Experiment and EOD simulations were conducted for Tecnai TF20 Super Twin for the beam deflection coils in Fig. 5.1. Experiment and EOD simulations were performed by Dr. Ondřej L. Sháněl due to my limited access to the TEM at the R&D department of Thermo Fisher Scientific. The micro-CT scans were employed to precisely and non-destructively measure the misalignment angles of the deflection coils, see Fig. 5.2 and 5.3. Micro-CT scans were performed by Ing. František Zelenka. Subsequently, the misalignment angle ε and the varying half-angles were measured for all deflectors. The limited structural integrity of the winding and cracks in-between are observed. The values for upper and lower deflectors are summarized in Tab. 5.1 and 5.2. A disturbing fact is that the winding full-angles are not 120° or within the range of specified manufacturing inaccuracy ±2° and each half of the saddle coil windings has a different size. This will probably lead to parasitic 3-fold astigmatism. Nevertheless, it is assumed that all half-angles are $\vartheta_\varepsilon = 60°$ in simulations. So, the news calculation methods can be used.

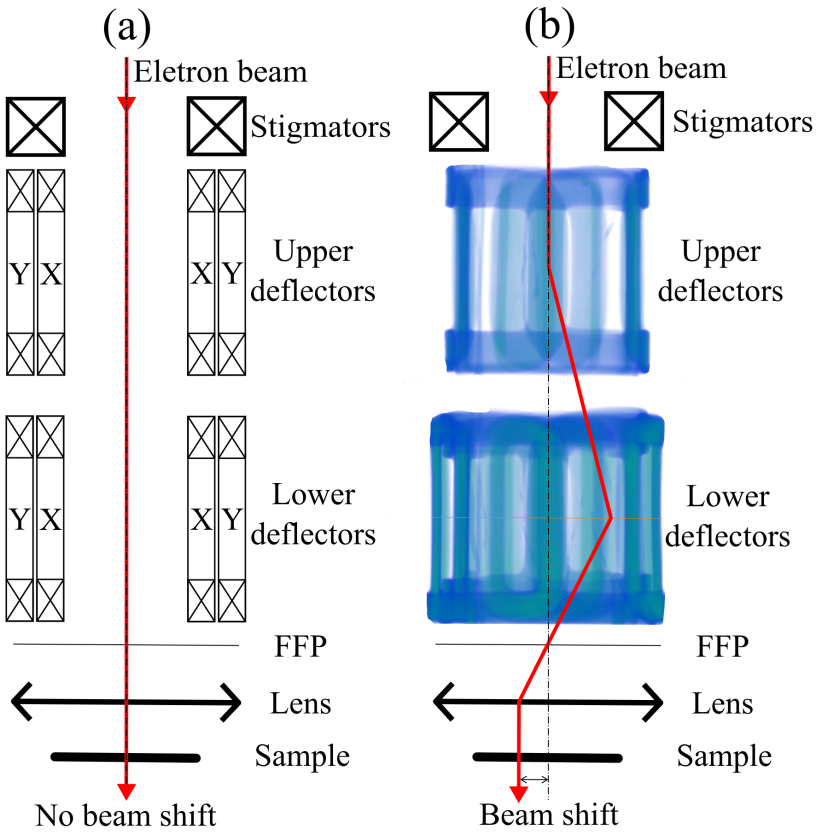

Fig. 5.1: A scheme of the electron-optical system of TEM Tecnai TF20 Super Twin used in the experiment. (a): First, the 2-fold astigmatism is minimized by stigmators. No current flows through the deflectors, the electron beam is not deflected. (b): Only X deflectors are used to deflect the electron beam to the front focal point (FFP) of the objective lens. Thus, the electron beam is shifted and propagates perpendicularly to the sample. The 2-fold astigmatism of the misaligned X deflectors is observed. The deflection system is represented by its image from the X-ray micro-tomography (micro-CT).

The Tecnai system was fully calibrated according to standard alignment procedure (accuracy for shift <1.5 % of the nominal value). The 2-fold astigmatism was calibrated

via stigmator current and readout of the condenser astigmatism on the ronchigram. Then, beam shift 1 µm by X-deflector was performed. So, only X-deflectors were used. Astigmatism measurement for the shifted beam was read out via the change of condenser stigmator current.

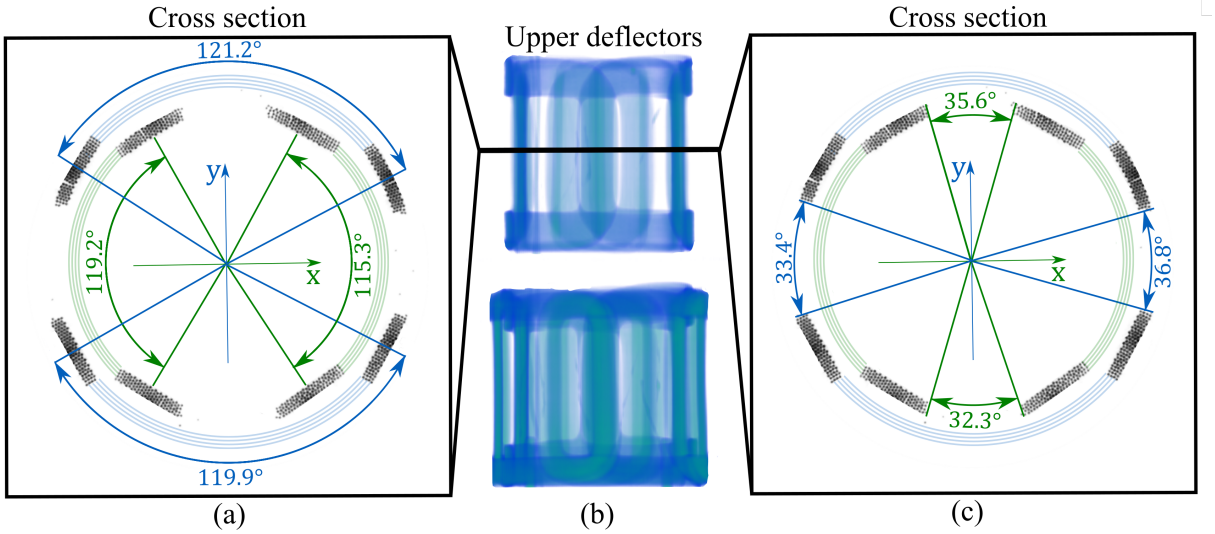

Fig. 5.2: (a): Micro-CT cross-section of the upper saddle coil deflectors. Full-angles of the X (green color) deflectors are $2v_{upper,X} = 115.3 \pm 0.3°$ and $2w_{upper,X} = 119.2 \pm 0.3°$. Full-angles of the Y (blue color) deflectors are $2v_{upper,Y} = 121.2 \pm 0.3°$ and $2w_{upper,Y} = 119.9 \pm 0.3°$. (b): Micro-CT of the upper saddle coil deflectors. (c): Micro-CT cross-section of the upper saddle coil deflectors to measure the misalignment angles ε. Some dimensions of the deflection system are not mentioned due to the company secret policy.

Table 5.1: Angles of the misaligned upper saddle coils

	Upper X deflector	Upper Y deflector
Misalignment angle ε	$\varepsilon_{upper,X} = -1.7 \pm 0.2°$	$\varepsilon_{upper,Y} = -1.7 \pm 0.2°$
Half-angle v	$v_{upper,X} = 57.65 \pm 0.15°$	$v_{upper,Y} = 60.60 \pm 0.15°$
Half-angle w	$w_{upper,X} = 59.60 \pm 0.15°$	$w_{upper,Y} = 59.95 \pm 0.15°$

Table 5.2: Angles of the misaligned lower saddle coils

	Lower X deflector	Lower Y deflector
Misalignment angle ε	$\varepsilon_{lower,X} = -0.6 \pm 0.2°$	$\varepsilon_{lower,Y} = -1.3 \pm 0.2°$
Half-angle v	$v_{lower,X} = 58.95 \pm 0.15°$	$v_{lower,Y} = 60.5 \pm 0.15°$
Half-angle w	$w_{lower,X} = 59.5 \pm 0.15°$	$w_{lower,Y} = 60.8 \pm 0.15°$

Simulations were performed in EOD 5.010. At first, only the deflection by the ideal deflectors was simulated. Then, additional fields simulating the non-ideal beam deflection coils system (both upper and lower) were introduced according to measured data from the micro-CT tomogram and their field representation in the corrected multipole method

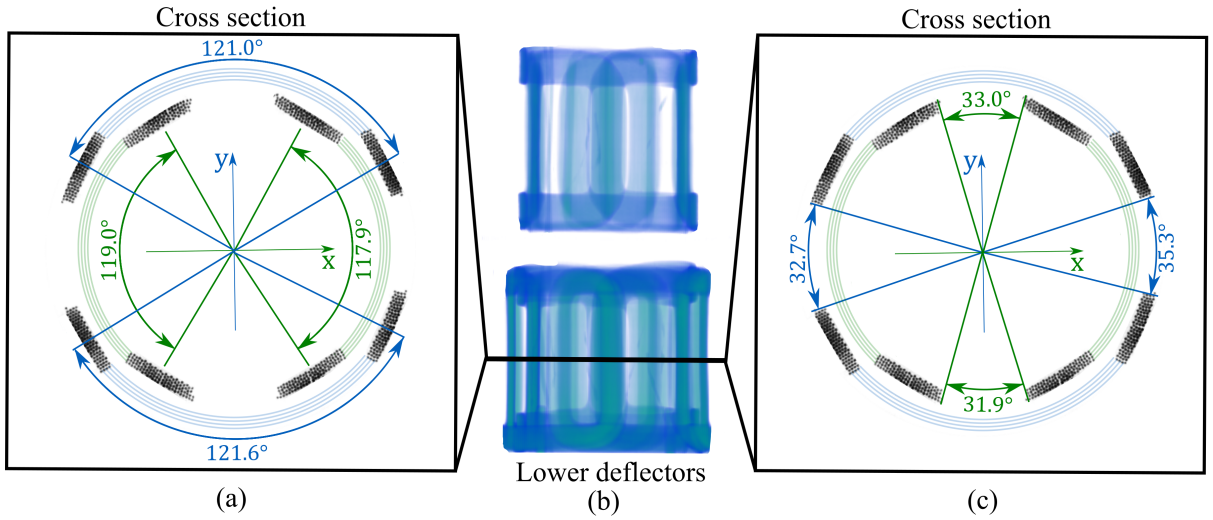

Fig. 5.3: (a): Micro-CT cross-section of the lower saddle coil deflectors. Full-angles of the X (green color) deflectors are $2v_{lower,X} = 117.9 \pm 0.3°$ and $2w_{lower,X} = 119.0 \pm 0.3°$. Full-angles of the Y (blue color) deflectors are $2v_{lower,Y} = 121.0 \pm 0.3°$ and $2w_{lower,Y} = 121.6 \pm 0.3°$. (b): Micro-CT of the lower saddle coil deflectors. (c): Micro-CT cross-section of the lower saddle coil deflectors to measure the misalignment angles ε. Some dimensions of the deflection system are not mentioned due to the company secret policy.

– see Tab. 5.3 and Tab. 5.4. Excitation for 1 µm beam shift in the X-deflector axis was calculated and applied to all correction fields. The beam spot of the ideal and non-ideal system in the eucentric plane of the objective lens is shown in Fig. 5.4 (a).

The total error of the beam position due to the deflectors and stigmators astigmatism Δw_a is expressed as

$$\Delta w_a = \Delta w_{a,def} + \Delta w_{a,stig} = k_a \bar{\alpha} \gamma^2 + A_a \alpha \tag{5.1}$$

where $\Delta w_{a,def}$ error position due to the deflectors' astigmatism, $\Delta w_{a,stig}$ error position due to the stigmators' astigmatism, k_a the astigmatism coefficient of deflectors. $\bar{\alpha}$ is complex conjugate of angles $\alpha = \alpha_x + \mathrm{i}\alpha_y$ where α_x is angle of particle with respect to optical axis z in plane xz and α_y in plane yz. γ is deflection of the beam and A_a is axial astigmatism of the stigmators. Then, total astigmatism of the system for the deflection γ is

$$A_c = k_a \gamma^2 + A_a. \tag{5.2}$$

Fig. 5.4 (b) shows calculated additional coma and 2-fold astigmatism caused by the non-ideal, misaligned deflection system. It was calculated by subtracting the two spots. It is important to realize that the main objective lens is magnetic. It rotates the electron beam from its original X-axis deflection to the eucentric plane (roughly in the center of the objective lens). The detailed EOD model of the TEM Tecnai TF20 Super Twin is not shared due to the company's secret policy. The results are summarized in Tab. 5.5.

5.1. The corrected multipole method

Tab. 5.3 and Tab. 5.4 content the parameters for simulation of the misaligned Xdeflection coils according to the corrected multipole method in EOD software. Half-angles are considered to be $\vartheta_\varepsilon = 60°$. Calculated according to the eq. (3.48) and (3.51).

Table 5.3: Angles $\vartheta_{m,\cos}$ and $\vartheta_{m,\sin}$ of the misaligned upper X saddle coil for the corrected multipole method. The misalignment angle is $\varepsilon_{upper,X} = -1.7 \pm 0.2°$.

Multipole fields	m	$\vartheta_{m,\cos}$ [°]	$\vartheta_{m,\sin}$ [°]	α_m [°]
Dipole fields	1	59.979	−0.714	90
Quadrupole fields	2	−0.0103	−0.357	45

Table 5.4: Angles $\vartheta_{m,\cos}$ and $\vartheta_{m,\sin}$ of the misaligned lower X saddle coil for the corrected multipole method. The misalignment angle is $\varepsilon_{lower,X} = -0.6 \pm 0.2°$.

Multipole fields	m	$\vartheta_{m,\cos}$ [°]	$\vartheta_{m,\sin}$ [°]	α_m [°]
Dipole fields	1	59.998	−0.238	90
Quadrupole fields	2	−0.0011	−0.119	45

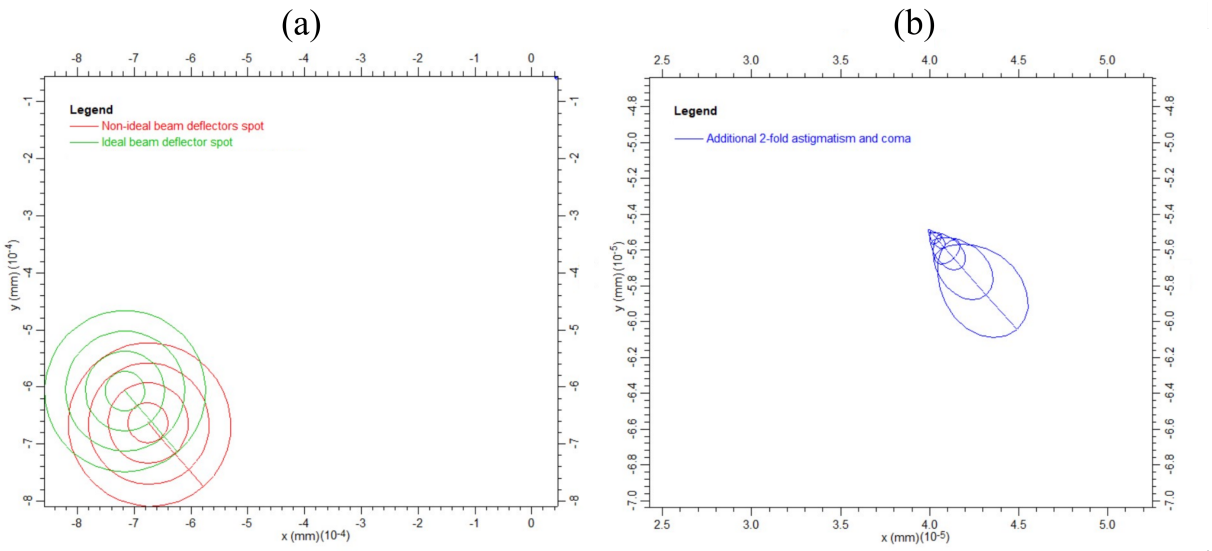

Fig. 5.4: (a): Spot position comparison for 1 µm shift in X-deflector axis. The electron beam is deflected by the ideal and non-ideal deflection system. (b): Additional coma and 2-fold astigmatism caused by the non-ideal, misaligned deflection system. Calculated by subtracting the two spots. Simulated by the module Combi in EOD software for the corrected multipole method for values in Table 5.3 and 5.4.

Table 5.5: Total astigmatism A_c of the TEM Tecnai TF20 Super Twin for deflection for the beam shift γ.

	Ideal system simulation	Non-ideal system simulation	Experiment
Beam shift γ [nm]	920	930	1000
Simulated A_c [nm]	0.382	53.5	49.0

Comparison of measured results

The calculated deviation of beam position caused by the ideal deflection system astigmatism is 0.382 nm for the beam shift 920 nm. The calculated deviation due to the astigmatisms is 53.5 nm for the non-ideal deflection coils and beam shift 930 nm. Measured deviation due to the astigmatisms is 49.2 nm for the experiment for the beam shift 1 µm. Therefore, the simulation corresponds well with the experiment. The difference can be explained by the limited accuracy of the 2-fold astigmatism readout on TEM Tecnai Super Twin 200kV (low-resolution camera) or by the measurement error of the misalignment angles. However, it is important to keep in mind that the corrected multipole method does not take into account the varying half-angles.

6. Conclusion

The manufacturing of saddle deflection coils routinely suffers from a lack of precision, ultimately leading to parasitic aberrations. In this thesis, I describe the effect of astigmatism of saddle coils due to the mechanical misalignment by deriving a general formula for calculating multipole field strength based on the angle of misalignment ε.

I implement novel methods for the multipole field calculations. Firstly, the normalized Fourier series coefficients method, and secondly, the corrected multipole method. Using the mentioned methods, the problem of the misaligned deflection coil reduces to the sum of fields of perfect multipole, for which there are already known solutions.

The mapping allows for an easy implementation in Electron Optic Design software, which has use in the manufacturing industry. The newly derived methods are ready to be used during the design of electron-optical systems by industrial subjects. This work gives a framework for the design of deflection systems aimed at mitigating 2-fold in electron microscopes.

Furthermore, the concept of the normalized Fourier series coefficients method could be applied to a general case of the misaligned multipole. The core principle could be suitable not only for the misalignment angle ε but also for the varying half-angles. Consequently, the application of the method could be broadened to the design process of quadrupole, hexapole, and octupole.

I have verified the results of the normalized Fourier series coefficients method and the corrected multipole method by directly comparing them with the 3D finite elements method. The relative difference between the compared methods is less than 3 % for the characteristic values, such as the global extrema and the integral value of multipole reduced axial magnetic potential.

The predicted astigmatism of the misaligned electron deflection system by the new calculation methods was also verified experimentally. The measured astigmatism of the saddle coils is in good agreement with the calculations. Moreover, the use of micro-CT to determine the misalignment was essential since it provided a detailed description of the manufacturing inaccuracy. The obtained measurements included the misalignment angle ε, varying half-angles, and cracks in-between the copper wires, which are encased in the resin.

Further research could focus on the effects of astigmatism due to the manufacturing inaccuracies in height, radius, cylindricity, and circularity of the saddle coil. I believe a complete theory of tolerances and misalignment aberrations is achievable and viable in practical settings. Influence on 3-fold and 4-fold astigmatism could be explore as well. The improvement of manufacturing precision of saddle coils could be an area of further interest and, possibly, lead to a new paradigm in the manufacturing technology of saddle coils.

In conclusion, this work introduces two new methods for calculating astigmatism in saddle deflection coils and provides a solid foundation for improving the off-axis resolution of transmission electron microscopes.

Bibliography

[1] BUSCH, H.; Berechnung der Bahn von Kathodenstrahlen im axialsymmetrischen elektromagnetischen Felde. *Annalen der Physik*, 386, no. 25 (1926): 974-993.

[2] BUSCH, H.; Über die Wirkungsweise der Konzentrierungsspule bei der Braunschen Röhre. *Archiv für Elektrotechnik*18, no. 6 (1927): 583-594.

[3] RUSKA, E.; The Development of the Electron Microscope and of Electron Microscopy. *Reviews of modern physics* 59, no. 3 (1987): 627.

[4] SCHERZER, O.; Über einige Fehler von Elektronenlinsen. *Zeitschrift für Physik*101, no. 9 (1936): 593-603.

[5] BOGNER, A.; A history of scanning electron microscopy developments: Towards "wet-STEM" imaging. *The Review of Scientific Instruments* 38, no. 4 (2007): 390-401.

[6] CREWE, A. V., et al.; Electron Gun Using a Field Emission Source. *Micron* 39, no. 4 (1968): 576-583.

[7] CREWE, A. V., Kopf, D. A.; Sextupole system for the correction of spherical aberration, *United States* (1980).

[8] *CEOS GmbH.* [online]. [cit. 2022-21-04]. Available from: `https://www.ceos-gmbh.de/en/about/max-haider`.

[9] The Nobel Prize in Physics 1986. In: *NobelPrize*, [online]. [cit. 2022-05-03]. Available from: `https://www.nobelprize.org/prizes/physics/1986/summary/`.

[10] NEWTON, I.; Philosophiae naturalis principia mathematica. *Jussu Societatis Regiae ac Typis Josephi Streater*. Prostat apud plures bibliopolas, 1687, page 12

[11] GRIFFITHS, D. J.; *Introduction to electrodynamics.* Upper Saddle River, N.J.: Prentice Hall, 1999.

[12] REIMER, L.; Scanning electron microscopy: physics of image formation and microanalysis. *2nd completely rev. and updated ed. New York: Springer* 1998. ISBN 978-3-540-63976-3.

[13] LENC, M.: *Optika nabitých částic.* Poznámky k přednášce v akademickém roce 2004/2005

[14] HAWKES, P. W., KASPER, E.; *Principles of Electron Optics: Volume 1, Basic Geometrical Optics*. London: Academic Press Limited, 1996. ISBN 978-1-4200-4554-3.

[15] SHÁNĚL, O.; *Tolerances and Misalignment Aberrations for Electron Optical Elements and Systems.*(doctoral thesis). Brno: Brno University of Technology, Faculty of Mechanical Engineering, 2014, 87 p.

[16] YUAN j., Et al.; An improved Helmholtz coil and analysis of its magnetic field homogeneity. *Review of Scientific Instruments* 73, no. 5 (2002): 2175-2179.

[17] YUAN J., et al.; A double-focusing Helmholtz-coil spectrometer. *Nuclear Instruments and Methods in Physics Research Section A: Accelerators, Spectrometers, Detectors and Associated Equipment* Volume 465, Issue 2–3, 2001, Pages 404-413. ISSN 0168-9002

[18] GINSBERG D. M., MELCHNER M. J.; Optimum Geometry of Saddle Shaped Coils for Generating a Uniform Magnetic Field. *The Review of Scientific Instruments*, Volume 41, Number 1, January 1970, Pages 122-123.

[19] Helmholtz coil. In: *Wikipedia*, [online]. [cit. 2022-05-03]. Available from: `https://en.wikipedia.org/wiki/Helmholtz_coil`

[20] LENC M., LENCOVÁ B.,; Analytical and numerical computation of multipole components of magnetic deflectors. *Review of Scientific Instruments* 68, no. 12 (1997): 4409-4414.

[21] LENCOVÁ, B., ZLÁMAL, J.; A new program for the design of electron microscopes. *Physics Procedia*, 2008, vol. 1, p. 315–324. ISSN 1875-389

[22] *COMSOL Multiphysics* [online]. [cit. 2022-01-26] <http://www.comsol.com/>

[23] ORLOFF, J.: *Handbook of Charged Particle Optics.* Boca Raton: CRC Press, 2009. ISBN 978-1-4200-4554-3.

[24] HORÁK, M., BADIN, v., ZLÁMAL, J.; Accurate interpolation of 3D fields in charged particle optics. *Ultramicroscopy* 189 (2018): 95-101.

[25] SEROV, V.: *Fourier Series, Fourier Transform and Their Applications to Mathematical Physics.* Springer, Cham, 2017, Volume 197 ISBN : 978-3-319-65261-0